Accepted Manuscript

Geological Society, London, Special Publications

Thermochronological constraints on the exhumation history of the Carboniferous Katebasu gold deposit, western Tianshan Gold Belt, NW China

WeiCe Zhao, XiaoBo Zhao, ChunJi Xue, Reimar Seltmann, Alla Dolgopolova, Jens C. Andersen, XinJie Cui & Ling Xing

Thermochronological constraints on the exhumation history of the Carboniferous Katebasu gold deposit, western Tianshan Gold Belt, NW China

WeiCe Zhao [1], XiaoBo Zhao [1, 2] *, ChunJi Xue [1] *, Reimar Seltmann [2], Alla Dolgopolova [2], Jens C. Andersen [3], XinJie Cui [1] & Ling Xing [4]

[1] State Key Laboratory of Geological Processes and Mineral Resources, Faculty of Earth Sciences and Resources, China University of Geosciences, Beijing 100083, China

[2] Center for Russian and Central Eurasian Mineral Studies, Department of Earth Sciences, Natural History Museum, Cromwell Road, London SW7 5BD, UK

[3] Camborne School of Mines, University of Exeter, Penryn Campus, Tremough, Penryn TR10 9FE, UK

[4] No. 1 Geological Survey Party, Xinjiang Bureau of Geology and Mineral Exploration and Mining, Urumqi 830011, China

* Correspondences (*e-mails:* xiaobozhao@cugb.edu.cn, chunji.xue@cugb.edu.cn)

Abstract: The western Tianshan Gold Belt hosts numerous giant and large gold deposits that have been formed during the late Paleozoic amalgamation of the Tianshan orogen. However, little is known about their exhumation histories during the Mesozoic to Cenozoic intracontinental evolution of the orogen. The Carboniferous Katebasu orogenic gold deposit in northwestern China is a new gold discovery within the western Tianshan Gold Belt, and it shares many similarities with other orogenic gold deposits in the belt. In this contribution, new ^{40}Ar/^{39}Ar and (U–Th)/He ages were combined with previous geochronology and

numerical modeling to quantify its post-Carboniferous cooling and exhumation history. The results revealed a three-phase cooling history and two phases of post-mineralization exhumation. We suggest that a large volume (~0.8 km) of the mineralized roof parts of the Katebasu deposit might have been removed during uplift and erosion, whereas significant ore reserves could still exist at depth. The large erosion depth of the Katebasu gold deposit in the Nalati Range of the Chinese western Tianshan also signifies that shallow-emplaced porphyry and epithermal systems that formed prior to Permo-Triassic uplift might have been largely eroded.

Introduction

Tracing the exhumation history of gold deposit is essential to understand when and how the buried orebodies were exposed to the paleosurface, as well as providing important information on ore potential at depth. The post-mineralization exhumation and exposure of hypogenic gold deposits could be better understood by utilizing low temperature thermochronological studies (McInnes et al. 2005). The most commonly used and effective methods include the zircon and apatite fission track and (U–Th)/He dating (traditionally abbreviated as ZFT, AFT, ZHe and AHe, respectively). Among these, the ZHe and AHe thermochronometers are sensitive to low temperatures of 170–200 °C (Reiners et al. 2004) and 40–85 °C (Wolf et al. 1998; Farley 2002), respectively, spanning the low temperature history after the formation of ore deposits, and therefore providing important insights on their preservation processes. In addition, a thermal history that spans over 800 °C from magmatic emplacement and hydrothermal activity to exhumation can be expected in combination with other independent geochronometers, i.e., U–Pb, Re–Os and ^{40}Ar/^{39}Ar systems (McInnes et al. 2005). This integrated approach has been applied widely to constrain the exhumation process and preservation conditions of epizonal to hypozonal orogenic gold deposits (Zhao 2016; Liu et al. 2017; Zhang et al. 2019a), as well as other types of gold deposits, i.e., porphyry and epithermal Au deposits (Márton et al. 2010; Leng et al. 2018) and Carlin-type Au deposits (Zeng et al. 2013) in Mesozoic and younger orogenic belts.

The Katebasu orogenic gold deposit (87 t proved Au reserves at a cut-off grade of 3.84 g/t; Zhang et al. 2015) is a large structurally-controlled orogenic gold deposit that

discovered in 2008 in the Nalati Range of the western Tianshan orogen in NW China (Fig. 1). The Chinese western Tianshan orogen is suggested to form the eastern extension of the Tianshan Gold Belt (TGB; Wall et al. 2004; Xue et al. 2014; Fig. 1b) extending from Uzbekistan Kyzylkum to Gobi Desert in northern China. The TGB is well known for its metal endowment with several giant and world-class gold deposits, such as Muruntau (> 5000 t Au) and Kumtor (> 570 t Au). Most of these gold deposits occur close to or directly within the regional fault zones and / or ductile-brittle shear zones within the accretionary collages of the western Tianshan orogen (Yakubchuk et al. 2002; Zhao et al. 2019). Their formation involved Paleozoic multiple episodes of accretion and the late Paleozoic amalgamation of the Paleo-Asian Ocean, followed by protracted Mesozoic to Cenozoic intracontinental deformation and uplift in response to the Eurasia-India amalgamation (Windley et al. 2007; Biske & Seltmann 2010; Xiao et al. 2013). Extensive geochronological dating during the last decades has shown that large-scale gold mineralization of the TGB took place in the late Paleozoic (Goldfarb et al. 2014; Xue et al. 2014), coinciding with the final amalgamation of the western Tianshan orogen (Biske & Seltmann 2010; Han & Zhao 2018). However, the Mesozoic to Cenozoic exhumation histories and exposure of these gold deposits remains enigmatic, due to lack of systematic low temperature thermochronology investigations on the gold deposits.

In this paper, we report new ^{40}Ar/^{39}Ar in hydrothermal sericite and (U–Th)/He in zircon and apatite datasets from the Katebasu fault-controlled gold deposit. In combination with previously published geochronological data and numerical modeling, we seek to quantify and reconstruct the magmatic to hydrothermal cooling and post-mineralization exhumation processes of the deposit. Our results advance understanding of the exhumation history of the western Tianshan orogen and shed new insights into future gold exploration in ancient orogenic belts.

Geological settings

Regional geology

The western Tianshan orogen lies in the southwestern part of the Central Asian Orogenic Belt (CAOB; Fig. 1a; Han et al. 2011). It is tectonically divided into the North, Middle and South Tianshan, which are separated by the Nikolaev Line – North Nalati Fault and the

Turkestan – Atbashi – Inylchek Fault (Fig. 1b), respectively (Gao et al. 2009; Biske & Seltmann 2010; Xue et al. 2014). The Katebasu gold deposit is located at the northern margin of the Chinese Middle Tianshan, adjacent to the Nikolaev Line – North Nalati Fault (Fig. 1b–c).

The Chinese Middle Tianshan is generally regarded as the eastern extension of the Uzbekistan and Kyrgyzstan Middle Tianshan (Fig. 1b; Gao et al. 2009; Xue et al. 2014). The tectonic evolution of the Chinese Middle Tianshan is characterized by two subduction systems in different directions along its northern and southern margins (Qian et al. 2009; Biske & Seltmann 2010; Xu et al. 2013), i.e., the Terskey Ocean to the north and the South Tianshan Ocean (also called Turkestan Ocean) to the south. Its basement is suggested to have been formed in the Paleo- to Mesoproterozoic according to previous geochronological and zircon Hf isotopic results (Huang et al. 2017; Long and Huang 2017). The basement rocks are unconformably overlain by Ordovician–Silurian intermediate–mafic volcanic rocks intercalated with carbonate and clastic formations (Charvet et al. 2011).

The early Paleozoic closure of the Terskey Ocean resulted in the formation of the Nikolaev Line – North Nalati Fault in the northern margin of the Middle Tianshan (Bazhenov et al. 2003; Qian et al. 2009; F_2 in Figure 2) and voluminous ~516–430 Ma arc-related magmatic rocks throughout the Chinese Middle Tianshan (Konopelko et al. 2008; Gao et al. 2009; Zhong et al. 2017). The subduction of the Terskey Ocean beneath the Middle Tianshan lasted to the earliest Silurian as indicated by the Middle Ordovician–Early Silurian (~465–443 Ma) island-arc granite (Glorie et al. 2010). In contrast, the late Paleozoic suture in the south of the Middle Tianshan, namely the Turkestan – Atbashi – Inylchek – South Nalati Fault, was formed from the closure of the Turkestan Ocean and subsequent collision orogeny of the western Tianshan (Gao et al. 2009; Biske & Seltmann 2010; Wang et al. 2011). The northward subduction of the Turkestan Ocean beneath the Middle Tianshan led to extensive Devonian–Carboniferous subduction-related magmatism in Uzbekistan and Kyrgyzstan (Chatkal–Kurama arc; Seltmann et al. 2011). The final closure of the South Tianshan Ocean is interpreted to have occurred in the Late Carboniferous (320–310 Ma; Han & Zhao 2018). Subsequently, the entire western Tianshan experienced a large-scale intracontinental dextral wrenching to accommodate the final amalgamation during the Permian, leading to the E–W dextral strike-slip and / or ductile shearing deformation and

regional uplifting and exhumation (De Jong et al. 2009; Charvet et al. 2011; Wang et al. 2018). During the Mesozoic and Cenozoic, the intracontinental deformation and the reactivation of inherited structures of the western Tianshan took place as a distal response to the Cimmerian Orogeny at the southern Eurasian margin and the India–Eurasia collision (De Grave et al. 2007; Glorie et al. 2011; Jepson et al. 2018). Multiple phases of exhumation in the Chinese Middle Tianshan have been recognized by previous thermochronological studies, including the Middle Triassic–Early Jurassic, the Late Jurassic–Early Cretaceous and the Eocene–Miocene (Fig. 1c; Jolivet et al. 2010; Wang et al. 2018; Yin et al. 2018; Zhang et al. 2019b).

Deposit geology and previous geochronological studies

Gold mineralization of the Katebasu deposit is mostly confined within an ENE-striking fracture zone intersecting the Carboniferous granitoids, that have intruded the Lower Silurian volcanic-sedimentary sequence (Fig. 2). Four major intrusive phases have been identified through field mapping, which include, from early to late, alkaline granite, monzogranite, granodiorite, and diorite and diorite porphyry (Figs. 2 and 3). Gold orebodies occur as steeply dipping, ENE-striking, lenticular and tabular forms (Fig. 2b) in the monzogranite that have experienced quartz, sericite and potassic alterations (Fig. 3f–h). Gold occurs mainly in the form of electrum and free gold along the margins of chalcopyrite or pyrite, and is also present as invisible gold within pyrite and chalcopyrite grains (Zhang et al. 2015).

The structural framework of the Katebasu gold deposit is characterized by a series of subparallel ENE–WSW-striking faults (Fig. 2a), which are generally regarded as secondary faults associated with reactivation of the Nikolaev Line – North Nalati Fault (F_2; Fig. 2a; Yang et al. 2013). Based on detailed structural mapping of the geometrics and kinematics of the faults, Zhao (2019) and Zhao et al. (2019) identified three major stages of deformation, including the Late Carboniferous top-to-the-north thrusting, Permian E–W-striking dextral strike-slip motion and post-Permian NE–SW-striking compressional deformation. The south-to-north thrusting resulted in a set of imbricated ENE-striking and S-dipping thrust faults, i.e., F_3, F_4, F_5, F_6 and F_7 faults (Fig. 2a). This stage of top-to-the-north thrusting appears to have a close relationship with gold mineralization and the development of fracture zone

between F_5 and F_6 faults, the main ore-hosting structures (Fig. 2a). Subsequently, the Permian dextral motion superimposed on the earlier ENE-striking faults lead to secondary dextral faults (F_8 and F_9) and conjugate NNW-striking sinistral faults (F_0, F_{11} and F_{12}; Fig. 2a). The later NE–SW-striking compressional deformation is represented by the NW-striking reverse fault (F_{10}) and NNE-striking dextral fault (F_{13}; Fig. 2a).

Several geochronological ages of the granitoids, hydrothermal alteration and mineralization have previously been published for the Katebasu gold deposit (Table 1). The earliest alkaline granite yielded U–Pb laser ablation inductively coupled plasma mass spectrometry (LA–ICP–MS) zircon age of 365.0 ± 4.2 Ma (Feng 2015). For the ore-hosting monzogranite, Feng et al. (2014) and Cai et al. (2019) have reported LA–ICP–MS U–Pb zircon crystallization ages of 346.3 ± 3.3 Ma and 350.4 ± 1.6 Ma, respectively. These ages are broadly coeval with dates from the same intrusion by secondary ion mass spectrometry (SIMS) and sensitive high mass resolution ion microprobe (SHRIMP) methods, which yielded U–Pb zircon ages of 351.4 ± 1.1 Ma (Dong et al. 2018) and 356.8 ± 5.2 Ma (Xing et al. 2015), respectively. The granodiorite and diorite have intruded almost simultaneously in the late stage, and they yielded LA–ICP–MS U–Pb zircon ages of 340.1 ± 1.8 Ma and 342.4 ± 3.6 Ma, respectively (Feng 2015). The timing of gold mineralization has been constrained to be 310.9 ± 4.2 Ma by Re–Os dating of auriferous pyrite (Zhang et al. 2015), although a much older age of 322.5 ± 6.8 Ma has also been obtained by Rb–Sr dating on pyrite grains (Dong et al. 2018).

Sampling and analytical methods

Sample selection

Samples for petrographic, $^{40}Ar/^{39}Ar$, AHe and ZHe thermochronological analysis were collected from diamond drill core and outcrop exposures at the Katebasu deposit area. Detailed sample locations are provided in Figure 2 and Table 2.

One sericite-altered monzogranite (1702KT; Fig. 3h) was selected for $^{40}Ar/^{39}Ar$ incremental step-heating analysis from a depth of 400 m in drill hole ZK1510 (Fig. 2a). Ten fresh monzogranite samples, including eight from outcrop exposure and two from drill hole ZK5112 (Fig. 2), were collected for AHe and ZHe thermochronological studies. They have an

average horizontal interval of 250 m, covering an elevation range from 2027 m to 2919 m (Table 2). A total of eight samples were selected for AHe dating and two samples were selected for ZHe dating. Mineral separates for $^{40}Ar/^{39}Ar$, AHe and ZHe dating were extracted from whole-rock samples using conventional magnetic and heavy liquid separation techniques. Individual separates were then hand-picked under a binocular microscope with purity up to 99.9% and examined under transmitted and reflected light.

Sericite $^{40}Ar/^{39}Ar$ dating

The separated hydrothermal sericite sample (1702KT) was cleaned ultrasonically using ethanol, and then sealed into a quartz bottle for irradiation along with the ZBH-25 biotite standard (132.7 ± 1.2 Ma at 1σ and a potassium content of 7.6 wt.%; Wang 1983) in the Swimming Pool Reactor of the Chinese Institute of Atomic Energy, Beijing. Total time for irradiation is 1440 min with a neutron flux of ca. 2.65×10^{13}n cm^{-2}S^{-1}, and the integrated neutron flux is 2.29×10^{18}n cm^{-2}. The irradiated sample and standard ZBH-25 biotite were stepwise heated from 600 °C to 1400 °C with each step for 10 minutes, followed by 20-minute purification. The isotopic analysis was performed using the Helix multiple collector mass spectrometer at the Institute of Geology, Chinese Academy of Geological Sciences (CAGS). Detailed procedures are reported by Chen et al. (2002). The measured isotopic ratios were corrected for system blanks, mass discrimination, interference isotopes and atmospheric argon. The K_2SO4 and CaF_2 produced during the irradiation were analyzed to obtain the interference isotope correction factors: $(^{36}Ar/^{37}Ar)_{Ca}= 0.0002398$, $(^{40}Ar/^{39}Ar)_K = 0.004782$ and $(^{39}Ar/^{37}Ar)_{Ca} = 0.000806$. All ^{37}Ar was corrected from radioactive decay and the ^{40}K decay constant was 5.543×10^{-10} year^{-1}. The ArArCALC program (Koppers 2012) was used to calculate the plateau and isochron ages and the uncertainties were reported at the 2σ level.

Apatite and zircon (U–Th)/He dating

Single crystals of apatite and zircon (3 to 4 crystals per sample) were used for AHe and ZHe dating. Prior to analysis, crystals were inspected under cross-polarized transmitted light to reject grains with invisible inclusions or internal fractures, and the selected grains were photographed and measured for the calculation of an alpha ejection correction factor (F_T; Farley 2000). AHe and ZHe dating of thirty-two apatite and seven zircon grains were

conducted at the Institute of Geology and Geophysics, Chinese Academy of Sciences (IGGCAS), following the standard analytical procedures described in Wu et al. (2016). Characterized apatite and zircon grains were then loaded into platinum and niobium microtubes, respectively, for helium extraction. Helium analyses were conducted using an automatic He extraction system named Alphachron MK II (Australian Scientific Instrument Pty Limited), which comprises a 970 nm diode laser, full-automatic gas purification line and a Quadruple Mass spectrometer. Multiple analysis suggested that a 10 A laser heating for five minutes (heated to 850–900 °C) was enough to extract > 99% [4]He in the heated apatite grains, while a 14 A laser heating for fifteen minutes (heated to 1000–1100 °C) was needed for zircon grains. The gas amount released by replicate heating was roughly the same as hot blank assured total extraction. Gas purification was completed with two SAES AP-10-N getters and helium was measured with a Quadruple Prisma Plus QMG 220. After [4]He extraction, the Pt wrapped grains were transferred to PFA vials for dissolution. The 25 μL solution, stored in 7 mol/L HNO_3 and contained 15 ng/mL U and 5 ng/mL Th, was added into each PFA vial. An ultrasonic washing for fifteen minutes and left at room temperature for four hours were very essential for complete dissolution. A total volume of 350 μL Milli-Q water were then added, and the solution was prepared for the measurement of U and Th in a Thermal Fisher X-Series II ICP-MS. Durango apatite and Fish Canyon Tuff (FCT) zircon, which were used as standards to monitor the analytical procedure, yielded average ages of 33.0 ± 2.2 Ma (2σ) and 26.8 ± 2.7 Ma (2σ), respectively, which are consistent with the ages obtained by other laboratories (Evans et al. 2005; Reiners 2005).

Inverse thermal modeling

In order to better constrain the thermal history of the Katebasu gold deposit, inverse thermal modeling has been performed using the HeFTy software (version 1.9.1; Ketcham 2005) on the basis of the new ZHe and AHe data from this study. The kinetic models of Farley (2000) and Reiners et al. (2004) were adopted for AHe and ZHe calculations, respectively, and other parameters are automatically set to corresponding default values (Table 3). The models were also constrained by sample elevation and present-day surface temperature (20 ± 10 °C) for outcrop samples, and sample depth and ambient temperature (assuming a current geothermal gradient of 25 °C/km; Wang et al. 1990) for drill hole samples. The published geochronological data and new thermochronological ages provide

vital time–temperature constraints on the models, and each model started at the time of gold mineralization that has been confined between 322.5 ± 6.8 Ma and 310.9 ± 4.2 Ma (Zhang et al. 2015; Dong et al. 2018). The corresponding initial temperature was set as ~200–400 °C which is normal for an orogenic gold deposit and is broadly consistent with previous micro-thermometric data of 281–335 °C of CO_2–H_2O fluid inclusions in quartz from gold-bearing quartz veins at Katebasu (Zhang et al. 2015). All the dated grains of each sample, except for the grains with age outliers, are incorporated in the model. The calculated weighted mean AHe and ZHe ages, as well as respective closure temperatures (T_c) of 170–200 °C (Reiners et al. 2004) and 40–85 °C (Wolf et al. 1998; Farley 2002), were used to constrain the timing of samples residing within the helium partial retention zone (HePRZ). The ending constraints were set as 0 Ma and present-day temperature. During the modeling, the Monte-Carlo simulation method was applied to generate and evaluate numerous independent and random time–temperature paths in result of 10,000 runs. The inverse modeling results were expressed in the form of path envelopes. The magenta envelope encompasses all good paths with goodness of fit larger than 0.50, while the green one represents a statistically acceptable path, which has a goodness of fit larger than 0.05. In addition, a weighted mean time–temperature path (in yellow line) was obtained and represents the most proximal thermal history.

Results

Sericite $^{40}Ar/^{39}Ar$ age

Hydrothermal sericite (# 1702KT) $^{40}Ar/^{39}Ar$ data are presented in Table 4, and age spectrum is shown in Fig. 4. The data reflects relatively well-resolved plateaus comprising 63.67% of the total ^{39}Ar released, and it shows identical plateau (333.77 ± 3.75 Ma) and inverse isochron age (336.26 ± 6.53 Ma).

(U–Th)/He ages

The AHe and ZHe data are presented in Tables 5 and 6, respectively. Thirty-two single grain AHe ages, ranging from 199.1 ± 10.4 Ma to 13.7 ± 0.7 Ma (Fig. 5a), were obtained from eight monzogranite samples. In general, single grain AHe ages show large intra-sample variations that exceed the analytical precision of 2.5% (Wu et al. 2016). Two monzogranite samples

yielded seven single grain ZHe ages varying from 322.9 ± 20.1 Ma to 260.7 ± 16.5 Ma. These samples also show large intra-sample age variations, which are also beyond the analytical uncertainty of 6.0%.

To avoid potential influence of outliers on averaging ages of the analyzed samples, the Chauvenet criterion was utilized for outlier detection. This method has been commonly used to reject ZHe and AHe outliers in previous thermochronological studies (Fitzgerald et al. 2006; Liu et al. 2017; Leng et al. 2018). Consequently, four single grain AHe ages from samples 17KT02, 17KT09, 17KT13 and 17KT15, respectively, failed the Chauvenet criterion test and were excluded from the determination of the weighted mean ages (Tables 5 and 6). Especially noteworthy is that the samples 17KT06 and 17KT22 show excessive scattered intra-sample single grain AHe ages and an error range well beyond analytical uncertainties (Tables 5 and 6). In such cases, the analytical uncertainties on individual ages indicate that intra-sample single grain AHe ages are not reliable, and so are the weighted mean ages calculated based on these ages (Green & Duddy 2018). Therefore, no weighted mean ages were calculated for these two samples.

HeFTy modeling results

The AHe ages of samples 17KT06 and 17KT22 are not reliable to perform the inverse modelling due to its high scattered intra-sample AHe ages (Green & Duddy 2018), and samples 17KT02 and 17KT21 cannot yield enough (less than 30) good time–temperature paths. The HeFTy thermal modeling (Ketcham 2005) results of the other six samples are plotted in Figure 6. The analyzed apatite grains in the ore-hosting monzogranite samples experienced a prolonged period within the apatite helium partial retention zone (AHePRZ; Fig. 6a–d), and slowly passed through the AHePRZ at rates of ~0.74–1.20 °C/Ma during the Early Jurassic to Late Cretaceous. Contrarily, the modelling from ZHe ages showed that sample 17KT07 fast passed through the zircon helium partial retention zone (ZHePRZ) at a higher average rate of ~10.35 °C/Ma during the Late Carboniferous to Early Permian. However, the sample experienced a decrease to ~4.77 °C/Ma cooling rate within the ZHePRZ (Fig. 6e). Sample 17KT17 passed through the ZHePRZ at an average rate of ~3.41 °C/Ma in the Early Permian (Fig. 6f).

Discussion

Evaluation of the (U–Th)/He data

The thermochronological data of all the samples from the Katebasu deposit show relatively large variations for the intra-sample single grain AHe and ZHe ages that exceed the relevant analytical errors (Tables 5 and 6). Potential factors accounting for the age dispersion include grain morphology (Brown et al. 2013), differences in grain size (Farley 2000; Reiners & Farley 2001), implantation of ^{4}He from neighboring U- or Th-rich mineral phases (Spencer et al. 2004; Spiegel et al. 2009), the existence of undetected U- or Th-rich mineral or fluid inclusions or excess ^{4}He in fluid inclusions (Farley 2002), U and Th heterogeneous distribution (Meesters & Dunai 2002; Hourigan et al. 2005; Farley et al. 2011), ^{4}He derived from radioactive decay of ^{147}Sm (Fitzgerald et al. 2006), radiation damage effect (Shuster et al. 2006; Flower et al. 2009; Guenthner et al. 2013) and cooling rate (Fitzgerald et al. 2006).

Prismatic grains are perfect objects for the AHe and ZHe analyses of single grain aliquots, while theoretical age variation resulted from analyzed broken grains can report age dispersion up to 40% of more (Brown et al. 2013). Compared to integrated grains with two terminations (2T), those broken grains can be clearly indicated by the common occurrences of only one or no clear terminations (1T or 0T) present on separated grains (Brown et al. 2013). Most of the dated apatite grains show no termination, except for one grain with one termination (Table 5; Fig. 7a), indicating that broken apatite grains are mainly responsible for the intra-sample single grain AHe age dispersion. Large grains have larger He diffusion domains (Farley, 2000), and thus leading to higher He closure temperatures with older AHe and ZHe ages (Reiners and Farley, 2001). The apatite grains from the Katebasu samples show no positive correlations between equivalent spherical radiuses (Res) and AHe ages (Fig. 7a), precluding the effect of variations in grain size on intra-sample dispersion of single grain AHe ages. The absence of U- or Th-rich mineral phases observed near apatite grains argue against the presence of He implantation. Except for some outliers, the general linear correlations between He concentration and effective U content (eU), which is equal to U concentration plus 0.235 times Th concentration (eU = [U] + 0.235 * [Th]), can exclude the presence of inclusions and excess ^{4}He (Fig. 7b). The heterogeneous distribution of parental nuclide in grains may affect the F_T correction, which will further induce dispersed AHe ages, even though the grains are from the same sample (Fitzgerald et al. 2006). As pointed by Farley et al. (2011), a maximum of 15% age difference can be produced between rim U-

enriched and core U-enriched apatite crystals. Such an extreme estimation of age variations is still insufficient to be responsible for the significantly dispersed ages in the Katebasu samples (Fig. 7a). The alpha decay of [147]Sm may increase He concentration in apatite and zircon grains, and thus can result in a systematic overestimation of corresponding AHe and ZHe ages. Reiners & Nicolescu (2006) demonstrated that 5% of radiogenic [4]He can be introduced by the alpha decay of [147]Sm, only if the U concentrations are less than 5 ppm. However, except for one sample with relatively low U concentration (3.8 ppm), all the other analyzed apatite grains in this study show U concentrations higher than 5 ppm (Table 5). Therefore, radioactive [4]He derived from [147]Sm is not the dominant factor to cause the widely scattered AHe ages. Radiation damage generally create isolated spaces in grains and can therefore affect He diffusion rates (Farley 2002; Reiners 2005). Previous studies have shown that radiation damage in apatite reduces He diffusivity, especially for samples that have experienced slow cooling and a prolonged period within the AHePRZ (Shuster et al. 2006; Flower et al. 2009). The AHe ages of four samples, i.e., 17KT03, 17KT06, 17KT09 and 17KT21, are positively correlated with eU (Fig. 7c), which indicate the effect of radiation damage on intra-sample AHe age variations. The other four samples do not show positive correlations, precluding the effect of radiation damage. If the samples are slowly cooled or retained within the AHePRZ for a protracted period, He diffusion can lead to variable degrees of He concentration for different-sized crystals, and thus to the greater variation of the AHe and ZHe ages (Leng et al. 2018). Also, Fitzgerald et al. (2006) suggested that the age variations in single grain AHe and ZHe ages under lower cooling rate (less than 3.0 °C/Ma) is much greater than it would be at higher cooling rates. The thermal modeling results at Katebasu indicated prolonged period and extremely slow cooling (less than 3.0 °C/Ma) since the Early Permian (Fig. 6), which probably contribute to the significant variation in the single grain AHe ages.

The intra-sample single grain ZHe ages are relatively more consistent than single grain AHe ages. The integrated zircon grains with two terminations (2T; Table 5; Fig. 7d), no positive correlations between equivalent spherical radiuses and ZHe ages (Fig. 7d), no U- or Th-rich mineral phases nearby and general linear correlations between He concentration and eU (Fig. 7e), exclude the effects of broken grain, variations in grain size, He implantation, inclusions and excess [4]He on the single grain ZHe age variations. The

heterogeneous distribution of parental nuclide and alpha decay of [147]Sm can also be excluded, similar to the case of apatite grains. Guenthner et al. (2013) indicated that low dosage of radiation damage for zircon could reduce He diffusivity rates and produce positive correlations between ZHe age and eU, whereas high dosage could significantly increase He diffusion rates and result in a negative correlation between ZHe age and eU. Sample 17KT17 shows a negative correlation between the ZHe ages and eU, indicating the effect of radiation damage (Fig. 7f), while sample 17KT07 do not have a negative correlation, indicating no radiation damage. In addition, the cooling rate is likely not responsible for the ZHe age variations due to the high cooling rates of the samples (Fig. 6e–f).

In summary, broken apatite grains and slow cooling, especially the former, are likely the crucial factors related to the intra-sample single grain AHe age variations. In addition, the radiation damage may partly affect both AHe and ZHe age variations.

Magmatic to hydrothermal cooling and mineralization

The application of multiple chronometers in gold deposits is essential for understanding the duration of magmatic–hydrothermal evolution, as well as the post-mineralization exhumation process that finally leads to the exposure of orebodies (McInnes et al. 2005). Commonly, the emplacement timing of a magmatic intrusion dated by U–Pb zircon method represents the commencement of a magmatic–hydrothermal event, [40]Ar/[39]Ar dates of potassium-rich alteration minerals provide the age of hydrothermal alteration or the lower-temperature limit of magmatic–hydrothermal event (Chiaradia et al. 2013). The ZHe system with closure temperatures of 170–200 °C (Reiners et al. 2004) can record the termination of mineralization and alteration events or the beginning of post-mineralization exhumation (Fu et al. 2010), whereas the AHe system with the lowest closure temperatures (40–85 °C; Farley 2002) have been used to temporally constrain the final cooling and exhumation. Our new [40]Ar/[39]Ar, AHe and ZHe data (Tables 4–6), combined with published geochronological data of the Katebasu gold deposit, were compiled to quantify the thermochronological history of the gold mineralization system (Fig. 8).

The magmatism at Katebasu has been suggested to initiate at ~365 Ma as indicated by detailed geological mapping and LA–ICP–MS zircon U–Pb dating on the alkaline granite (Feng 2015), which represents the earliest intrusive phase in the region. However, as gold

mineralization is mostly confined into the monzogranite, the time–temperature curve obtained from the monzogranite and associated mineralization and alteration may therefore provide the cooling history of the gold deposit. In general, the Katebasu gold deposit has experienced a protracted, three-phase cooling history from magmatic–hydrothermal to exhumation stage since the Early Carboniferous (Fig. 8). The emplacement of the ore-hosting monzogranite has occurred ~356.8–346.3 Ma (LA–ICP–MS, SHRIMP and SIMS zircon U–Pb ages; Feng et al. 2014; Xing et al. 2015; Dong et al. 2018). A similar emplacement age of 350.4 ± 1.6 Ma has been reported for the ore-hosting monzogranite by using LA–ICP–MS zircon U–Pb method, and the crystallization temperatures of ~765–975 °C for zircons from monzogranite has also been obtained from titanium-in-zircon thermometer (Cai et al. 2019). The new hydrothermal sericite $^{40}Ar/^{39}Ar$ plateau age of 333.8 ± 3.8 Ma from the ore-hosting monzogranite (Fig. 4) indicate the late stage of high-temperature hydrothermal fluids at Katebasu. Considering the closure temperature of ~300–360 °C for the sericite $^{40}Ar/^{39}Ar$ system (Hames and Bowring 1994), it is estimated that the magmatic–hydrothermal system at Katebasu experienced a phase of faster cooling with temperatures dropping from ~765–975 °C to ~300–360 °C during the Early Carboniferous. The calculated duration and average rate for this phase of faster cooling can be up to 12.5 to 23.0 million years at an average rate of ~31.03 °C/Ma (Fig. 8). This cooling rate is significantly lower than the magmatic cooling rate of a porphyry system, which could typically be up to hundreds of degrees per million year (°C/Ma; McInnes et al. 2005; Fu et al. 2010). In the western TGB, only few authors have investigated cooling and exhumation history from a deposit / district scale (Zhao et al. 2020), and examples for orogenic gold deposits has not been reported yet in the region. Globally, the cooling rates of the magmatic–hydrothermal stage for the orogenic gold deposits at the Jiaodong province in eastern China have been estimated to be tens of degrees per million year (°C/Ma; Yang et al. 2016; Zhao 2016; Zhang et al. 2019b), which is in agreement with our estimation of ~31.03 °C/Ma for Katebasu. The long duration of the high-temperature magmatic-hydrothermal event at Katebasu could be likely attributed to thermal effects of other late intrusions which include the granodiorite (~340.1 Ma; Feng 2015) and the diorite (~342.4 Ma; Feng 2015). It is supposed to be resulted from an incrementally constructed plutonic system that feeds the upper crustal intrusive complex (Chiaradia et al. 2013).

Auriferous pyrite Re–Os isochron age of 310.9 ± 4.2 Ma (Zhang et al. 2015) and Rb–Sr isochron age of 322.5 ± 6.8 Ma for pyrite grains (Dong et al. 2018) have been presented to constrain the timing of the main gold mineralization at Katebasu, and previous micro-thermometric data of CO_2–H_2O fluid inclusions in quartz from gold-bearing quartz veins has constrained the mineralization temperature to be of 281–335 °C (Zhang et al. 2015). These indicate that the precipitation of gold veins occurred during the transition from late stage of high-temperature hydrothermal stage to medium-temperature hydrothermal stage, which has been constrained by the temperatures of hydrothermal sericite $^{40}Ar/^{39}Ar$ system (300–360 °C; Hames and Bowring 1994) and the gold mineralization (281–335 °C; Zhang et al. 2015).

Since the mineralization temperature of 281–335 °C (Zhang et al. 2015) is higher than the closure temperature of ZHe system (170–200 °C; Reiners et al. 2004), the ZHe ages obtained in this study are believed to record the timing of initial post-mineralization uplifting and exhumation at Katebasu (McInnes et al. 2005). Therefore, it is suggested that the deposit has experienced a phase of moderate cooling immediately after gold mineralization during the Late Carboniferous to Early Permian, as recognized by time–temperature curve (Fig. 8), which likely coincides with regional uplifting and exhumation resulting from collisional orogeny in the Chinese Middle Tianshan (Wang et al. 2018; Yin et al. 2018). During this period, the gold orebodies were likely cooled accompanied with uplifting with an average cooling rate estimated to be ~4.38 °C/Ma. This phase of moderate cooling coincides with our modelling results which show that the samples passed through the ZHePRZ during the Late Carboniferous to Early Permian (Fig. 6e–f). Following this moderate cooling event, a protracted period of extremely slow cooling at an average rate of ~0.57 °C/Ma have occurred since the Early Permian to the present as constrained by the AHe ages and the modelling in this study (Figs. 6a–d and 8), which is consistent with the negative correlations between elevation and AHe ages of the samples (Fig. 5c). Collectively, the modeling results indicate that the Katebasu gold deposit has experienced two phases of exhumation (Fig. 9).

Exhumation history

Previous thermochronological studies on the Chinese Middle Tianshan has revealed a phase of rapid exhumation from the Late Carboniferous to the Early Permian, which has been interpreted to be associated with the amalgamation of the western Tianshan orogen (Jolivet et al. 2010; Wang et al. 2018; Yin et al. 2018). Our modeling from the ZHe ages of the Katebasu deposit also indicated a coherent faster exhumation event, which took the monzogranite to an average depth of ~6.0 km during the Permian (~294–263 Ma). The average exhumation rate was estimated to be up to ~0.208 km/m.y. if we adopted a paleo-geothermal gradient of 25 °C/km (Fig. 9). Subsequently, the modelling from the AHe ages indicated a phase of slow exhumation at an average rate of ~0.037 km/m.y., which took the monzogranite to an average depth of ~1.8 km during the Early Jurassic to Late Cretaceous (~193–66 Ma). Since then, the exhumation rate decreased as the thermal modelling indicated a slight decrease of cooling rate (Fig. 6a–d). According to our new AHe and ZHe ages and corresponding closure temperatures, the average erosion rate of country rocks can be estimated to be ~0.024 km/m.y. (Fu et al. 2010), and thus the eroded thickness of country rocks can be calculated to be ~2.6 km since the Early Jurassic to Late Cretaceous (~193–66 Ma). These calculations suggest an average eroded thickness of ~0.8 km of the ore-hosting monzogranite after the exposure of the Katebasu deposit (Fig. 9).

The rate of the Late Carboniferous–Early Permian exhumation is slightly faster than the estimated average exhumation rate of simultaneous regional exhumation in the Chinese western Tianshan, which has been reported to be of ~0.102–0.180 km/m.y. (Lv et al. 2013; Zhang et al. 2019a). Comparatively, the exhumation rates of the orogenic gold deposits at Jiaodong province have been estimated to be up to ~0.131 km/m.y. at most (Liu et al. 2017). Therefore, the Late Carboniferous–Early Permian exhumation at Katebasu seems to be relatively faster, which might be attributed to the Late Carboniferous collisional orogen and subsequent intense dextral wrenching (De Jong et al. 2009; Charvet et al. 2011; Han & Zhao 2018; Wang et al. 2018; Zhang et al. 2019b). The rate of the Mesozoic slow exhumation at Katebasu is consistent with the regional exhumation in the western TGB (Lv et al. 2013; Yu et al. 2016; Zhang et al. 2016, 2019b; Wang et al. 2018) and the Jiaodong orogenic gold province (Lv et al. 2013; Zhang et al. 2019a).

Exploration implications

Gold mineralization of the Katebasu deposit is primarily controlled by a series of ENE-striking faults and associated fracture systems adjacent to the Nikolaev Line – North Nalati trans-crustal fault zone (Fig. 1; Zhao et al. 2019), and shares similarities with other fault-controlled orogenic gold deposits in the western TGB (Wall et al. 2004; Goldfarb et al. 2014; Xue et al. 2014). However, its current reserves are much smaller than those of the giant gold deposits in the western TGB, such as Muruntau (> 5000 t Au) and Kumtor (> 570 t Au; Yakubchuk et al. 2002). According to previous micro-thermometric data of CO_2–H_2O fluid inclusions from gold-bearing quartz veins at Katebasu (Zhang et al. 2015), an estimated mineralization depth was indicated to be less than ~11.0 km. In the western TGB, many orogenic gold deposits are known to have a mesozonal mineralization depths similar to Katebasu. Based on fluid inclusions micro-thermometric estimation from auriferous quartz veins, the Saridala gold deposit (36 t Au) at the Chinese Middle Tianshan (Fig. 1b) is estimated to have occurred at a depth of ~11 km (Zhang et al. 2018). Similarly, the Sawaya'erdun gold deposit (130 t Au) in the Chinese South Tianshan (Fig. 1b) is reported to be have been formed at the depths up to ~8 km (Chen et al. 2012). The mineralization depth of the Jilau gold deposit (110 t Au) in the Tajik South Tianshan (Fig. 1b) is suggested to be of ~7–10 km (Cole et al. 2000). From a global perspective, meso- and hypozonal orogenic gold deposits are widely reported. Gold mineralization at the Jiaodong orogenic gold province in eastern China has been confined to be formed at the depths of ~6–11 km according to thermochronological studies on the ore-hosting granitoids (Zhao 2016). The large Charlotte gold mine (144 t Au) in western Australia has been constrained to be formed at a depth of ~10 km by micro-thermometric data of fluid inclusions from quartz veins (Mueller 2015). In addition, Kolb et al. (2015) reported ~10–16 km mineralization depths of several hypozonal orogenic gold deposits, i.e., New Consort (South Africa), Renco (Zimbabwe), Klein Labata (South Africa), Hutti and Kolar (India), Nevoria (western Australia), and The Granites (Northern Territory, Australia). Actually, the mineralization depth of fault-controlled orogenic deposits worldwide could extend to be up to 20 km (Groves et al. 1998). Considering that gold mineralization at Katebasu has a controlled maximum dip of 1085 m and still extends downward without pinching out (Zhang et al. 2015), we suggest that although ~0.8 km thick orebodies at Katebasu may have been removed during uplift and erosion, significant gold reserves could still exist at depths. The large erosion depth of the Katebasu is expected to be beneficial for the formation of placer gold deposits nearby.

However, no significant placer gold has been found yet in the Nalati Range. The only two small placer deposits (Tiange'er and Houxia; Au resources of 2.17 t), ca. 270 km far away from the Katebasu deposit (Fig. 1b), are suggested to be originated from the Saridala and the adjacent Wangfeng orogenic gold deposits (Rui et al. 2002). Comparatively, significant placer gold deposits have been mined for decades in both Chinese Altay and the northern Karakorum to the north and south of the Chinese western Tianshan (Rui et al. 2002; Zhou et al. 2002). In addition to abundant gold sources and beneficial transport medium, rapid accumulation of the overlying sediments has been proved to benefit the preservation of these placer gold (Wang and Zhao, 2006). Therefore, it is suggested that the intense regional neo-tectonism since the Early Mesozoic may be responsible for the scarcity of placer gold deposits in the Nalati Range of the Chinese Middle Tianshan.

Equally important, shallow-emplaced porphyry and epithermal systems in the Nalati Range that formed prior to Permo-Triassic uplift might have been largely eroded. This is consistent with the fact that no porphyry or epithermal deposits have been discovered to date in the Chinese Middle Tianshan, but significant porphyry Cu and related epithermal Au deposits occur in the Uzbekistan Middle Tianshan (e.g., Almalyk district) with its eastern extension to Kyrgyzstan and China that have experienced different exhumation histories (Jepson et al. 2018). Post-mineralization exhumation processes played a significant role in controlling the size and tonnage of preserved magmatic–hydrothermal deposits in ancient orogenic belts.

Conclusions

New $^{40}Ar/^{39}Ar$, AHe and ZHe data combined with previously published geochronometers and numerical modeling allowed to quantify the cooling and exhumation processes of the Katebasu fault-controlled orogenic gold deposit in the Chinese western Tianshan. A three-phase cooling history was recognized at Katebasu, which includes first phase of faster cooling (~31.03 °C/Ma) in the Early Carboniferous, a second phase of moderate cooling (~4.38 °C/Ma) in the Late Carboniferous to Early Permian, and a prolonged period of slow cooling since the Early Permian (~0.57 °C/Ma). Overall, two phases of post-mineralization exhumation can be identified based on our modeling results. The first phase of faster exhumation (an average rate of ~0.208 km/m.y.) was likely caused by the

regional collisional orogeny during the Late Carboniferous to Early Permian. The second phase of slow exhumation was related to surface erosion with an average rate of ~0.037 km/m.y. since the Early Permian. Coupled uplift and erosion might have removed a large volume (~0.8 km thick) of the mineralized roof parts of the Katebasu deposit, however, significant ore reserves could still be preserved at depths (> 1.0 km).

References

Bazhenov, M.L., Collins, A.Q., Degtyarev, K.E., Levashova, N.M., Mikolaichuk, A.V., Pavlov, V.E. and Van der Voo, R. 2003. Paleozoic northward drift of the North Tien Shan (Central Asia) as revealed by Ordovician and Carboniferous paleomagnetism. *Tectonophysics*, **366**, 113–141.

Biske, Y.S. and Seltmann, R. 2010. Paleozoic Tian-Shan as a transitional region between the Rheic and Urals–Turkestan oceans. *Gondwana Research*, **17**, 602–613.

Brown, R.V., Beucher, R., Roper, S., Persano, C., Stuart, F. and Fitzgerald, P.G. 2013. Natural age dispersion arising from the analysis of broken crystals. Part I: theoretical basis and implications for the apatite (U–Th)/He thermochronometer. *Geochimica Cosmochimica Acta*, **122**, 478–497.

Cai, H.M., Liu, G.P., Nijat, A., Yang, W.Z. and Xing, L. 2019. U-Pb age and geochemistry of zircons from the Katebasu Au deposit, West Tianshan Mountains, Xinjiang, and their

geological implications. *Geological Bulletin of China*, **38(5)**, 790–801 (in Chinese with English abstract).

Charvet, J., Shu, L.S., Laurent-Charvet, S., Wang, B., Faure, M., Cluzel, D., Chen, Y. and de Jong, K. 2011. Palaeozoic tectonic evolution of the Tianshan belt, NW China. *Science China Earth Sciences*, **54(2)**, 166–184.

Chen, H.Y., Chen, Y.J. and Baker, M.J. 2012. Evolution of ore-forming fluids in the Sawayaerdun gold deposit in the Southwestern Chinese Tianshan metallogenic belt, Northwest China. *Journal of Asian Earth Sciences*, **49**, 131–144.

Chen, W., Liu, X.Y. and Zhang, S.H. 2002. Continuous laser stepwise heating ^{40}Ar/^{39}Ar dating technique. *Geological Review*, **48(Supp.)**, 127–134 (in Chinese with English abstract).

Chiaradia, M., Schaltegger, U., Spikings, R., Wotzlaw, J.F. and Ovtcharova, M. 2013. How Accurately Can We Date the Duration of Magmatic-Hydrothermal Events in Porphyry Systems — An Invited Paper. *Economic Geology*, **108**, 565–584.

Cole, A., Wilkinson, J.J., Halls, C. and Serenko, T.J. 2000. Geological characteristics, tectonic setting and preliminary interpretations of the Jilau gold–quartz vein deposit, Tajikistan. *Mineralium Deposita*, **35**, 600–618.

De Grave, J., Buslov, M.M., Van den haute, P. 2007. Distant effects of India-Eurasia convergence and Mesozoic intracontinental deformation in Central Asia: constraints from apatite fission track thermochronology. *Journal of Asian Earth Sciences*, **29**, 188–204.

De Jong, K., Wang, B., Faure, M., Shu, L. S., Cluzel, D., Charvet, J., Ruffet, G. and Chen, Y. 2009. New ^{40}Ar/^{39}Ar age constraints on the Late Palaeozoic tectonic evolution of the western Tianshan (Xinjiang, northwestern China), with emphasis on Permian fluid ingress. *International Journal of Earth Sciences*, **98**, 1239–1258.

Deng, J., Wang, C., Bagas, L., Carranza, E.J.M. and Lu, Y. 2015. Cretaceous–Cenozoic tectonic history of the Jiaojia Fault and gold mineralization in the Jiaodong Peninsula, China: constraints from zircon U–Pb, illite K–Ar, and apatite fission track thermochronometry. *Mineralium Deposita*, **50**, 987–1006.

Dong, L.L., Wan, B., Yang, W.Z., Deng, C., Chen, Z.Y., Yang, L., Cai, K.D. and Xiao, W.J. 2018. Rb–Sr geochronology of single gold-bearing pyrite grains from the Katbasu gold deposit in the South Tianshan, China and its geological significance. *Ore Geology Reviews*, **100**, 99–110.

Evans, N.J., Byrne, J.P., Keegan, J.T. and Dotter, L.E. 2005. Determination of uranium and thorium in zircon apatite and fluorite application to laser (U–Th) He Thermochronology. *Journal of Analytical Chemistry*, **60**, 1159–1165.

Farley, K.A. 2000. Helium diffusion from apatite: general behavior as illustrated by Durango fluorapatite. *Journal of Geophysical Research–Solid Earth*, **105**, 2903–2914.

Farley, K.A. 2002. (U–Th)/He dating: techniques, calibrations, and applications. *Reviews in Mineralogy and Geochemistry*, **47**, 819–844.

Farley, K.A., Shuster, D.L. and Ketcham, R.A. 2011. U and Th zonation in apatite observed by laser ablation ICPMS, and implications for the (U–Th)/He system. *Geochimica et Cosmochimica Acta*, **75**, 4515–4530.

Feng, B. 2015. *Geology and geochemistry of granitoid in Katebasu large Au deposit, Western Tianshan, and its relation to mineralization*. Master's thesis, China University of Geosciences (Beijing) (in Chinese with English abstract).

Feng, B., Xue, C.J., Zhao, X.B., Ding, Z.X., Zhang, Q., Zu, B., Yang, W.Z., Lin, Z.H. and Chen, W. 2014. Petrology, geochemistry and zircon U-Pb isotope chronology of monzogranite of the Katbasu Au-Cu deposit, western Tianshan, Xinjiang Province. *Earth Science Frontiers*, **21(5)**, 187–195 (in Chinese with English abstract).

Fitzgerald, P.G., Baldwin, S.L., Webb, L.E. and O'Sullivan, P.B. 2006. Interpretation of (U–Th)/He single grain ages from slowly cooled crustal terranes: A case study from the Transantarctic Mountains of southern Victoria Land. *Chemical Geology*, **225**, 91–120.

Flowers, R.M., Ketcham, R.A., Shuster, D.L. and O'Sullivan, P.B. 2009. Apatite (U–Th)/He thermochronometry using a radiation damage accumulation and annealing model. *Geochimica et Cosmochimica Acta*, **73**, 2347–2365.

Fu, F.Q., McInnes, B.I.A., Evans, N.J. and Davies, P.J. 2010. Numerical modeling of magmatic-hydrothermal systems constrained by U-Th-Pb-He time-temperature histories. *Journal of Geochemical Exploration*, **106**, 90–109.

Gao, J., Long, L.L., Klemd, R., Qian, Q., Liu, D.Y., Xiong, X.M., Su, W., Liu, W., Wang, Y.T. and Yang, F.Q. 2009. Tectonic evolution of the South Tianshan orogen and adjacent regions, NW China: geochemical and age constraints of granitoid rocks. *International Journal of Earth Sciences*, **98**, 1221–1238.

Glorie, S., De Grave, J., Buslov, M.M., Elburg, M.A., Stockli, D.F., Gerdes, A., and Van den haute, P. 2010. Multi-method chronometric constraints on the evolution of the Northern Kyrgyz Tien Shan granitoids (Central Asian Orogenic Belt): From emplacement to exhumation. *Journal of Asian Earth Sciences*, **38**, 131–146.

Glorie, S., De Grave, J., Buslov, M.M., Zhimulev, F.I., Stockli, D.F., Batalev, V.Y., Izmer, A., Van der haute, P., Vanhaecke, F. and Elburg, M.A. 2011. Tectonic history of the Kyrgyz South Tien Shan (Atbashi-Inylchek) suture zone: the role of inherited structures during deformation-propagation. *Tectonics*, **30(6)**, TC6016.

Goldfarb, R.J., Taylor, R.D., Collins, G.S., Goryachev, N.A. and Orlandini, O.F. 2014. Phanerozoic continental growth and gold metallogeny of Asia. *Gondwana Research*, **25**, 48–102.

Green, P. and Duddy, I. 2018. Apatite (U-Th-Sm)/He thermochronology on the wrong side of the tracks. *Chemical Geology*, **488**, 21–33.

Groves, D.I., Goldfarb, R.J., Gebre-Mariam, M., Hagemann, S. and Robert, F. 1998. Orogenic gold deposits: a proposed classification in the context of their crustal distribution and relationship to other gold deposit types. *Ore Geology Reviews*, **13**, 7–27.

Guenthner, W.R., Reiners, P.W., Ketcham, R.A., Nasdala, L. and Giester, G. 2013. Helium diffusion in natural zircon: Radiation damage, anisotropy, and the interpretation of zircon (U–Th)/He thermochronology. *American Journal of Science*, **313**, 145–198.

Hames, W.E. and Bowring, S.A. 1994. An empirical evaluation of the argon diffusion geometry in muscovite. *Earth and Planetary Science Letters*, **124**, 161–169.

Han, B.F., He, G.Q., Wang, X.C. and Guo, Z.J. 2011. Late Carboniferous collision between the Tarim and Kazakhstan-Yili terranes in the western segment of the South Tian Shan Orogen, Central Asia, and implications for the Northern Xinjiang, western China. *Earth-Science Reviews*, **109**, 74–93.

Han, Y.G. and Zhao, G.C. 2018. Final amalgamation of the Tianshan and Junggar orogenic collage in the southwestern Central Asian Orogenic Belt: Constraints on the closure of the Paleo-Asian Ocean. *Earth-Science Reviews*, **186**, 129–152.

Hourigan, J.K., Reiners, P.W. and Brandon, M.T. 2005. U-Th zonation dependent alpha-ejection in (U-Th)/He chronometry. *Geochimica et Cosmochimica Acta*, **69**, 3349–3365.

Huang, Z.Y., Long, X.P., Wang, X.C., Zhang, Y.Y., Du, L., Yuan, C. and Xiao, W.J. 2017. Precambrian evolution of the Chinese Central Tianshan Block: Constraints on its tectonic affinity to the Tarim Craton and responses to supercontinental cycles. *Precambrian Research*, **295**, 24–37.

Jepson, G., Glorie, S., Konopelko, D., Gillespie, J., Danišík, M., Mirkamalov, R., Mamadjanov, Y. and Collins, A.S. 2018. Low-Temperature Thermochronology of the Chatkal-Kurama Terrane (Uzbekistan-Tajikistan): Insights into the Meso-Cenozoic Thermal History of the Western Tian Shan. *Tectonics*, **37**, 3954–3969.

Jolivet, M., Dominguez, S., Charreau, J., Chen, Y., Li, Y.A. and Wang, Q.C. 2010. Mesozoic and Cenozoic tectonic history of the central Chinese Tian Shan: reactivated tectonic structures and active deformation. *Tectonics*, **29**, TC6019.

Ketcham, R.A. 2005. Forward and inverse modeling of low-temperature thermochronometry data. *Reviews in Mineralogy and Geochemistry*, **58**, 275–314.

Ketcham, R.A., Gautheron, C. and Tassan-Got, L. 2011. Accounting for long alpha-particle stopping distances in (U-Th-Sm)/He geochronology: Refinement of the baseline case. *Geochimica et Cosmochimica Acta*, **75**, 7779–7791.

Kolb, J., Dziggel, A. and Bagas, L. 2015. Hypozonal lode gold deposits: a genetic concept based on a review of the New Consort, Hutti, Hira Buddini, Navachab, Nevoria, and The Granites deposits. *Precambrian Research*, **262**, 20–44.

Konopelko, D., Biske, G., Seltmann, R., Kiseleva, M., Matukov, D. and Sergeev, S. 2008. Deciphering Caledonian events: Timing and geochemistry of the Caledonian magmatic arc in the Kyrgyz Tien Shan. *Journal of Asian Earth Sciences*, **32**, 131–141.

Koppers, A.A.P. 2002. ArArCALC—software for ^{40}Ar/^{39}Ar age calculations. *Computers & Geosciences*, **28(5)**, 605–619.

Leng, C.B., Cooke, D.R., Hou, Z.Q., Evans, N.J., Zhang, X.C., Chen, W.T., Danišik, M., McInnes, B.I.A. and Yang, J.H. 2018. Quantifying Exhumation at the Giant Pulang Porphyry Cu-Au Deposit: Using U-Pb-He Dating. *Economic Geology*, **113**, 1077–1092.

Liu, X., Fan, H.R., Evans, N.J., Yang, K.F., Danišik, M., McInnes, B.I.A., Qin, K.Z. and Yu, X.F. 2017. Exhumation history of the Sanshandao Au deposit, Jiaodong: Constraints from structural analysis and (U–Th)/He thermochronology. *Scientific Reports* 7(7787), DOI: 10.1038/s41598-017-08103-w

Long, X.P. and Huang, Z.Y. 2017. Tectonic affinities of microcontinents in the Central Asian Orogenic Belt: A case study of the Chinese Tianshan Orogenic Belt. *Bulletin of Mineralogy, Petrology and Geochemistry*, **36(5)**, 771–785 (in Chinese with English abstract).

Lv, H.H., Chang, Y., Wang, W. and Zhou, Z.Y. 2013. Rapid exhumation of the Tianshan Mountains since the Early Miocene: Evidence from combined apatite fission track and (U–Th)/He thermochronology. *Science China: Earth Sciences*, **43**, 1964–1974 (in Chinese).

Márton, I., Moritz, R. and Spikings, R. 2010. Application of low-temperature thermochronology to hydrothermal ore deposits: Formation, preservation and exhumation of epithermal gold systems from the Eastern Rhodopes, Bulgaria. *Tectonophysics*, **483(3–4)**, 240–254.

McInnes, B.I.A., Evans, N.J., Fu, F.Q. and Garwin, S. 2005. Application of thermochronology to hydrothermal ore deposits. *Reviews in Mineralogy and Geochemistry*, **58**, 467–498.

Meesters, A.G.C.A. and Dunai, T.J. 2002. Solving the production-diffusion equation for finite diffusion domains of various shapes Part II: Application to cases with a-ejection and nonhomogeneous distribution of source. *Chemical Geology*, **186**, 347–363.

Mueller, A.G. 2015. Structure, alteration, and geochemistry of the Charlotte quartz vein stockwork, Mt Charlotte gold mine, Kalgoorlie, Australia: time constraints, down-plunge zonation, and fluid source. *Mineralium Deposita*, **50**, 221–244.

Qian, Q., Gao, J., Klemd, R., He, G.Q., Song, B., Liu, D.Y. and Xu, R.H. 2009. Early Paleozoic tectonic evolution of the Chinese South Tianshan Orogen: constraints from SHRIMP zircon U–Pb geochronology and geochemistry of basaltic and dioritic rocks from Xiate, NW China. *International Journal of Earth Sciences*, **98**, 551–569.

Reiners, P.W. 2005. Zircon (U–Th)/He thermochronometry. *Reviews in Mineralogy and Geochemistry*, **58**, 151–179.

Reiners, P.W. and Farley, K.A. 2001. Influence of crystal size on apatite (U–Th)/he thermochronology: an example from the Bighorn Mountains, Wyoming. *Earth and Planetary Science Letters*, **188 (3)**, 413–420.

Reiners, P.W. and Nicolescu, S. 2006. Measurement of parent nuclides for (U–Th)/He chronometry by solution sector ICP-MS. ARHDL Report.1.

Reiners, P.W., Spell, T.L., Nicolescu, S. and Zanetti, K.A. 2004. Zircon (U–Th)/He thermochronometry, He diffusion and comparisons with ^{40}Ar/^{39}Ar dating. *Geochimica Cosmochimica Acta*, **68**, 1857–1887.

Rui, Z.Y., Goldfarb, R.J., Qiu, Y.M., Zhou, T.H., Chen, R.Y., Pirajno, F. and Yun, G. 2002. Paleozoic–early Mesozoic gold deposits of the Xinjiang Autonomous Region, northwestern China. *Mineralium Deposita*, **37**, 393–418.

Seltmann, R., Konopelko, D., Biske, G., Divaev, F. and Sergeev, S. 2011. Hercynian postcollisional magmatism in the context of Paleozoic magmatic evolution of the Tien Shan orogenic belt. *Journal of Asian Earth Sciences*, **42**, 821–838.

Shuster, D.L., Flowers, R.M. and Farley, K.A. 2006. The influence of natural radiation damage on helium diffusion kinetics in apatite. *Earth and Planetary Science Letters*, **249**, 148–161.

Soloviev, S.G., Kryazhev, S. and Dvurechenskaya, S. 2018. Geology, mineralization, and fluid inclusion study of the Kuru-Tegerek Au-Cu-Mo skarn deposit in the Middle Tien Shan, Kyrgyzstan. *Mineralium Deposita*, **53**, 195–223.

Spencer, A.S., Kohn, B.P., Gleadow, A.J.W., Norman, M., Belton, D.X. and Carter, T.J. 2004. The importance of residing in a good neighbourhood: rechecking the rules of the game for apatite (U–Th)/He thermochronology. *In:* Andressien, P. *(eds) 10th International Fission track Dating Conference*. Amsterdam, Netherlands, 20.

Spiegel, C., Kohn, B.L., Belton, D.X., Berner, Z. and Gleadow, A.J.W. 2009. Apatite (U–Th–Sm)/He thermochronology of rapidly cooled samples: the effect of He implantation. *Earth and Planetary Science Letters*, **285**, 105–114.

Wall, V.J., Graupner, T., Yantsen, V., Seltmann, R., Hall, G.C. and Muhling, J. 2004. Muruntau, Uzbekistan: a giant thermal aureole gold (TAG) system. *In:* Muhling, J., Goldfarb, R., Vielreicher, N., Bierlein, F., Stumpfl, E., Groves, D.I. and Kenworth, S. *(eds) SEG 2004: Predictive Mineral Discovery Under Cover-Extended Abstracts: Centre for Global Metallogeny*. University of Western Australia, Australia, 199–203.

Wang, B., Shu, L.S., Faure, M., Jahn, B.M., Cluzel, D., Charvet, J., Chung, S.L. and Meffre, S. 2011. Paleozoic tectonics of the southern Chinese Tianshan: Insights from structural, chronological and geochemical studies of the Heiyingshan ophiolitic mélange (NW China). *Tectonophysics*, **497**, 85–104.

Wang, J., Huang, S.Y., Huang, G.S. and Wang, J.Y. 1990. Basic characteristics of the earth's temperature distribution in China. Geological Publishing House, Beijing, China (in Chinese).

Wang, S.S. 1983. Age determinations of ^{40}Ar–^{40}K, ^{40}Ar–^{39}Ar and radiogenic ^{40}Ar released characteristics on K–Ar geostandards of China. *Chinese Journal of Geology*, **4**, 315–323 (in Chinese with English abstract).

Wang, Y.B. and Zhao, D.J. 2006. Gold deposits in Xinjiang, China. Geological Publishing House, Beijing, China (in Chinese).

Wang, Y.N., Cai, K.D., Sun, M., Xiao, W.J., De Grave, J., Wan, B. and Bao, Z.H. 2018. Tracking the multi-stage exhumation history of the western Chinese Tianshan by apatite fission track (AFT) dating: Implication for the preservation of epithermal deposits in the ancient orogenic belt. *Ore Geology Reviews*, **100**, 111–132.

Windley, B.F., Alexeiev, D., Xiao, W.J., Kröner, A. and Badarch, G. 2007. Tectonic models for accretion of the Central Asian Orogenic Belt. *Journal of the Geological Society, London*, **164**, 31–47.

Wolf, R.A., Farley, K.A. and Kass, D.M. 1998. A sensitivity analysis of the apatite (U-Th)/He thermochrometer. *Chemical Geology*, **148**, 105–114.

Wu, L., Monié, P., Wang, F., Lin, W., Ji, W.B., Bonno, M., Münch, P. and Wang, Q.C. 2016. Cenozoic exhumation history of Sulu terrane: Implications from (U–Th)/He thermochronology. *Tectonophysics*, **672–673**, 1–15.

Xiao, W.J., Windley, B.F., Allen, M. and Han, C.M. 2013. Paleozoic multiple accretionary and collisional tectonics of the Chinese Tianshan orogenic collage. *Gondwana Research*, **23**, 1316–1341.

Xing, L., Yang, W. Z., Zang, M., Lin, Z. H. and Chen, W. 2015. Zircon SHRIMP U–Pb dating of the monzonitic granite from Kateba'asu Au–Cu deposit and its geological implications in Xin Jing. *Xinjiang Geology*, **33(1)**, 1–6 (in Chinese with English abstract).

Xu, X.Y., Wang, H.L., Li, P., Chen, J.L., Ma, Z.P., Zhu, T., Wang, N. and Dong, Y.P. 2013. Geochemistry and geochronology of Paleozoic intrusions in the Nalati (Narati) area in western Tianshan, Xinjiang, China: Implications for Paleozoic tectonic evolution. *Journal of Asian Earth Sciences*, **72**, 33–62.

Xue, C.J., Zhao, X.B., Mo, X.X., Dong, L.H., Gu, X.X., Nurtaev, B., Pak, N., Zhang, Z.C., Wang, X.L. ZU, B., Zhang, G.Z., Feng, B. and Liu J.Y. 2014. Asian Gold Belt in western Tianshan and its dynamic settings, metallogenic control and exploration. *Earth Science Frontiers*, **21(5)**, 128–155 (in Chinese with English abstract).

Yakubchuk, A., Cole, A., Seltmann, R. and Shatov, V. 2002. Tectonic setting, characteristics, and regional exploration criteria for gold mineralization in the Altaid orogenic collage: the Tien Shan province as a key example. *Special Publication–Society of Economic Geologists*, **9**, 177–202.

Yang, L.Q., Deng, J., Wang, Z.L., Zhang, L., Goldfarb, R.J., Yuan, W.M., Weinberg, R.F. and Zhang, R.Z. 2016. Thermochronologic constraints on evolution of the Linglong Metamorphic Core Complex and implications for gold mineralization: a case study from the Xiadian gold deposit, Jiaodong Peninsula, eastern China. *Ore Geology Reviews*, **72**, 165–178.

Yang, W.Z., Xue, C.J., Zhao, X.B., Zhao, S.M., Wei, J., Feng, B., Zhou, H., Lin, Z.H., Zheng, H., Liu, J.W., Zhang, Q. and Zu, B. 2013. The discovery of the Kateba'asu large Au-Cu deposit in Xinyuan County, western Tianshan, Xinjiang. *Geological Bulletin of China*, **32(10)**, 1613–1620 (in Chinese with English abstract).

Yin, J.Y., Chen, W., Hodges, K.V., Xiao, W.J., Cai, K.D., Yuan, C., Sun, M., Liu, L.P. and van Soest, M.C. 2018. The thermal evolution of Chinese central Tianshan and its implications: Insights from multi-method chronometry. *Tectonophysics*, **722**, 536–548.

Yu, S., Chen, W., Zhang, B., Sun, J.B., Li, C., Yuan, X., Shen, Z., Yang, L. and Ma, S. 2016. Mesozoic and Cenozoic uplifting and exhumation history of the Kekesu section on the center Tianshan: constrained from (U-Th)/He thermochronometer. *Chinese Journal of Geophysics*, **59(8)**, 2922–2936 (in Chinese with English abstract).

Zeng, Q.T., Evans, N.J., McInnes, B.I.A., Batt, G.E., McCuaig, C.T., Bagas, L. and Tohver, E. 2013. Geological and thermochronological studies of the Dashui gold deposit, West Qinling Orogen, Central China. *Mineralium Deposita*, **48**, 397–412.

Zhang, B., Chen, W., Liu, J.Q., Yin, J.Y. and Sun, J.B. 2019b. Thermochronological insights into the intracontinental orogeny of the Chinese western Tianshan orogen. *Journal of Asian Earth Sciences*, https://doi.org/10.1016/j.jseaes.2019.103927.

Zhang, B., Chen, W., Sun, J.B., Yu, S., Yin, J.Y., Li, H., Zhang, Y., Liu, X.Y., Yang, L. and Yuan, X. 2016. The thermal history and uplift process of the Ouxidaban pluton in the South

Tianshan orogen: Evidence from Ar–Ar and (U–Th). *Science China: Earth Sciences*, **59**, 349–361 (in Chinese).

Zhang, L., Chen, H.Y., Liu, C.F. and Zheng, Y. 2018. Ore genesis of the Saridala gold deposit, Western Tianshan, NW China: Constraints from fluid inclusion, S-Pb isotopes and ^{40}Ar/^{39}Ar dating. *Ore Geology Reviews*, **100**, 63–76.

Zhang, L., Yang, L.Q., Weinberg, R.F., Groves, D.I., Wang, Z.L., Li, G.W., Liu, Y., Zhang, C. and Wang, Z.K. 2019a. Anatomy of a world-class epizonal orogenic-gold system: a holistic thermochronological analysis of the Xincheng gold deposit, Jiaodong Peninsula, eastern China. *Gondwana Research*, **70**, 50–70.

Zhang, Q., Xue, C.J., Zhao, X.B., Feng, B., Xing, H., Mo, X.X., Zhao, S.M., Yang, W.Z. and Xing, L. 2015. Geology, geochemistry and metallogenic epoch of the Katebasu large-sized gold deposit, Western Tianshan Mountains, Xinjiang. *Geology in China*, **42(3)**, 411–438 (in Chinese with English abstract).

Zhao, R. 2016. *Tectonic evolution and gold mineralization in the Jiaodong Peninsula*. Phd thesis, China University of Geosciences (Beijing) (in Chinese with English abstract).

Zhao, W.C., 2019. *Structural evolution and gold mineralization of the Katebasu gold deposit in the western Tianshan, China*. PhD thesis, China University of Geosciences (Beijing) (in Chinese with English abstract).

Zhao, W.C., Zhao, X.B., Xue, C.J., Symon, D.T.A., Cui, X.J. and Xing, L. 2019. Structural characterization of the Katebasu gold deposit, Xinjiang, China: Tectonic correlation with the amalgamation of the western Tianshan. *Ore Geology Reviews*, **107**, 888–902.

Zhao, X.B., Xue, C.J., Zhao, W.C., Seltmann, R., Symon, D.T.A., Dolgopolova, A. and Zhang, Y. 2020. Cooling and exhumation of the Late Paleozoic Tulasu epithermal gold system, Western Tianshan, NW China: implications for preservation of Pre-Mesozoic epithermal deposits. Journal of the Geological Society, DOI: https://doi.org/10.1144/jgs2020-099.

Zhong, L.L., Wang, B., Alexeiev, D.V., Cao, Y.C., Biske, Y.S., Liu, H.S., Zhai, Y.Z. and Xing, L.Z. 2017. Paleozoic multi-stage accretionary evolution of the SW Chinese Tianshan: new

constraints from plutonic complex in the Nalati Range. *Gondwana Research*, **45**, 254–274.

Zhou, T.H., Goldfarb, R.J. and Phillips, G.N. 2002. Tectonics and distribution of gold deposits in China – an overview. *Mineralium Deposita*, **37**, 249–282.

Figure captions

Fig. 1. (**a**) Tectonic schematic map of the Central Asian Orogenic Belt (modified from Han et al. 2011). (**b**) Simplified tectonic framework of the western Tianshan Orogen, with locations of major gold deposits (modified from Xue et al. 2014; Soloviev et al. 2018). (**c**) Simplified geological map of the Chinese western Tianshan orogen, showing ZHe and AHe data in literature (modified from Gao et al. 2009; Xu et al. 2013). The data have been reported by [1] Jolivet et al. (2010); [2] Lv et al. (2013); [3] Yu et al. (2016); [4] Zhang et al. (2016); [5] Yin et al. (2018); [6] Zhang et al. (2019b) and references therein. The blue bold and italic dates represent ZHe and AHe ages, respectively.

Fig. 2. Geological map (**a**) and KT51 exploration cross-section (**b**) of the Katebasu gold deposit, showing the locations of samples used for thermochronological study (modified from Zhang et al. 2015; Zhao et al. 2019).

Fig. 3. Representative photographs and photomicrographs of the granitoids and gold ore of the Katebasu gold deposit. (**a**) hand specimen of fresh alkaline granite. (**b**) hand specimen of fresh monzogranite. (**c**) hand specimen of granodiorite. (**d**) Alkaline granite has a coarse-grained equigranular texture with abundant K-feldspar, quartz, plagioclase, quartz and biotite under cross-polarized light. (**e**) Monzogranite (sample # 17KT02) with abundant plagioclase, K-feldspar, quartz and biotite under cross-polarized light. (**f**) Weakly sericite-altered granodiorite showing plagioclase and quartz under cross-polarized light. (**g**) Tabular orebody hosted within alteration zones in monzogranite. (**h**) mineralized monzogranite sample (sample # 1702KT) with intense potassic alteration. (**i**) Fine-grained sericite in the potassic-altered monzogranite sample under cross-polarized light. Abbreviations: Qtz, quartz; Kfs, K-feldspar; Pl, plagioclase; Bt, biotite; Py, pyrite; Ser, sericite.

Fig. 4. Sericite ^{40}Ar/^{39}Ar plateau age spectrum of the sample 1702KT from the Katebasu gold deposit.

Fig. 5. (**a**) Histogram of single grain AHe age distribution, and elevation versus single grain AHe (**b**) and ZHe ages (**b**) plots of the Katebasu gold deposit.

Fig. 6. Modeled time–temperature paths for the analyzed samples and published thermochronometers of the Katebasu deposit using HeFTy thermal modeling of Ketcham (2005). Yellow line represents the weighted mean time–temperature path, and magenta and green areas represent good paths (goodness-of-fit > 0.5) and acceptable paths (goodness-of-fit > 0.05), respectively. Abbreviations: AHePRZ, apatite helium partial retention zone; ZHePRZ, zircon helium partial retention zone.

Fig. 7. Plots of AHe ages vs. Res (**a**), ZHe ages vs. Res (**b**), apatite He concentrations vs. eU (**c**), zircon He concentrations vs. eU (**d**), AHe ages vs. eU (**e**) and ZHe ages vs. eU (**f**) for all the analyzed samples from the Katebasu gold deposit, together with insets of photomicrographs showing morphology of represented apatite and zircon grains for dating. Abbreviations: Res, equivalent spherical radius; [^{4}He], He concentration; eU, effective U concentration.

Fig. 8. Temperature–time path of the thermochronometers from the Katebasu gold deposit. The ZHe and AHe ages represent the averaging of all the single grain ZHe and AHe ages, except for the outliers, and the X-axis error bars represent the range of all the single grain ZHe and AHe ages, respectively. The value in the ellipse represents the average cooling rate (°C/Ma).

Fig. 9. Simplified diagram showing the uplift and exhumation processes of the Katebasu gold deposit.

Table captions

Table 1. *Summary of previous geochronological data of the Katebasu gold deposit*

Table 2. *Location and descriptions of samples used for hydrothermal sericite ^{40}Ar/^{39}Ar, zircon and apatite (U–Th)/He dating of the Katebasu gold deposit*

Table 3. *Parameters of inverse thermal modeling input into the HeFTy software (version 1.9.1)*

Table 4. *Hydrothermal sericite ^{40}Ar/^{39}Ar step-heating data of the Katebasu gold deposit*

Table 5. *Apatite (U–Th)/He results for samples of the Katebasu gold deposit*

Table 6. *Zircon (U–Th)/He results for samples of the Katebasu gold deposit*

Table 1. *Summary of previous geochronological data of the Katebasu gold deposit*

Host rock	Mineral	Dating method	Age (Ma, 2σ)	Reference
Alkaline granite	Zircon	U–Pb LA–ICP–MS	365.0 ± 4.2	Feng (2015)
Monzogranite	Zircon	U–Pb LA–ICP–MS	346.3 ± 3.3	Feng et al. (2014)
Monzogranite	Zircon	U–Pb SHRIMP	356.8 ± 5.2	Xing et al. (2015)
Monzogranite	Zircon	U–Pb SIMS	351.4 ± 1.1	Dong et al. (2018)
Monzogranite	Zircon	U–Pb LA–ICP–MS	350.4 ± 1.6	Cai et al. (2019)
Granodiorite	Zircon	U–Pb LA–ICP–MS	340.1 ± 1.8	Feng (2015)
Diorite	Zircon	U–Pb LA–ICP–MS	342.4 ± 3.6	Feng (2015)
Monzogranite	Pyrite	Rb–Sr TIMS	322.5 ± 6.8	Dong et al. (2018)
Gold ore	Pyrite	Re–Os N–TIMS	310.9 ± 4.2	Zhang et al. (2015)

Table 2. *Location and descriptions of samples used for hydrothermal sericite $^{40}Ar/^{39}Ar$, zircon and apatite (U–Th)/He dating of the Katebasu gold deposit*

Sample No.	Latitude (N), longitude(E) / drilling hole	Elevation	Mineral assemblage (volume percentage)	Dated mineral
1702KT	Drill hole ZK1510, 400 m depth	2416 m	Pl (~5%), Kfs (20–30%), Qtz (30–35%), Ser (10–15%), Py (5–8%) and Chl (~5%)	Sericite
17KT02	Surface, 43°09'11"N, 83°22'09"E	2627 m	Pl (30–35%), Kfs (35–40%), Qtz (~20%), Bt (3%) and minor apatite and magnetite	Apatite
17KT03	Surface, 43°08'59"N, 83°21'59"E	2649 m	Pl (35–40%), Kfs (30–35%), Qtz (15–20%), Bt (5%) and minor apatite and zircon	Apatite
17KT06	Surface, 43°08'51"N, 83°22'14"E	2483 m	Pl (30–35%), Kfs (30–35%), Qtz (~20%), Bt (5–10%) and minor apatite and zircon	Apatite
17KT09	Surface, 43°09'06"N, 83°22'46"E	2536 m	Pl (30–35%), Kfs (30–35%), Qtz (~20%), Bt (5%) and minor apatite and magnetite	Apatite
17KT13	Surface, 43°09'07"N, 83°23'49"E	2919 m	Pl (30–35%), Kfs (30–35%), Qtz (~20%), Bt (5%) and minor apatite and chlorite	Apatite
17KT15	Surface, 43°09'03"N, 83°23'32"E	2861 m	Pl (35–40%), Kfs (30–35%), Qtz (~20%), Bt (5%) and minor apatite and magnetite	Apatite
17KT21	Drill hole ZK5112, 400 m depth	2314 m	Pl (30–35%), Kfs (35–40%), Qtz (~20%), Bt (3%) and minor apatite and zircon	Apatite
17KT22	Drill hole ZK5112, 687 m depth	2027 m	Pl (30–35%), Kfs (35–40%), Qtz (~20%), Bt (3%) and minor zircon and apatite	Apatite
17KT07	Surface, 43°08'51"N, 83°22'42"E	2609 m	Pl (30–35%), Kfs (30–35%), Qtz (~20%), Bt (5–10%) and minor apatite and zircon	Zircon
17KT17	Surface, 43°08'57"N, 83°23'10"E	2827 m	Pl (30–35%), Kfs (35–40%), Qtz (~20%), Bt (3%) and minor zircon and apatite	Zircon

Coordinates of drill holes: ZK1510 (43°08'57"N, 83°22'53"E), ZK5112 (43°08'48"N, 83°22'42"E). Abbreviations: Pl, plagioclase; Kfs, K-feldspar; Qtz, quartz; Bt, biotite; Ser, sericite; Py, pyrite; Chl, chlorite

Table 3. *Parameters of inverse thermal modeling input into the HeFTy software (version 1.9.1)*

Parameter	Option / value for apatite	Option / value for zircon
Calibrations	Farley (2000)	Reiners et al. (2004)
Model precision	Best	Best
Geometry	Sphere	Sphere
Radius	Equivalent spherical radius	Equivalent spherical radius
E	32.9 kcal/mol	40.4 kcal/mol
D_0	50 cm^2/s	0.46 cm^2/s
E_t	6.93 kcal/mol	
ψ	1.26×10^{-4} g/nmol	
$E_{(N17)}$		16.97 kcal/mol
$D_{0(N17)}$		6.367×10^{-3} g/nmol
Stopping distances	Ketcham et al. (2011)	Ketcham et al. (2011)
Alpha calculation	Redistribution	Redistribution
Age to report	Corrected	Corrected
Age alpha correction	Ketcham et al. (2011)	Ketcham et al. (2011)

Notes: E, activation energy; D_0, frequency factor; E_t, activation energy for the apatite model of Farley (2000); ψ, frequency factor for the apatite model of Farley (2000); $E_{(N17)}$, activation energy for the zircon model of Reiners et al. (2004); $D_{0(N17)}$, frequency factor for the zircon model of Reiners et al. (2004).

Table 4. *Hydrothermal sericite $^{40}Ar/^{39}Ar$ step-heating data of the Katebasu gold deposit*

T (°C)	^{36}Ar [a]	^{37}Ar [Ca]	^{38}Ar [Cl]	^{39}Ar [K]	^{40}Ar[r]	^{40}Ar(r)/^{39}Ar(k)	^{40}Ar(r) (%)	^{39}Ar(k) (%)	Age (Ma)	± 2σ (Ma)
1702KT sericite: step = 13, mass = 16.21 mg, irradiation parameter = 0.00364598 ± 0.00001823										
600	0.0009378	0.0000000	0.0003775	0.0123202	0.63537	29.07446	56.38	0.29	181.77	6.58
700	0.0028686	0.0000000	0.0057671	0.4251911	22.59511	51.14264	96.24	10.06	308.49	0.98
750	0.0023251	0.0000647	0.0064534	0.4913796	27.68161	54.93147	97.51	11.62	329.38	0.99
780	0.0009984	0.0000000	0.0071476	0.5705282	32.12498	55.78555	99.07	13.49	334.06	1.01
820	0.0008744	0.0017929	0.0072689	0.5790354	32.44095	55.57518	99.20	13.70	332.91	1.00
860	0.0011419	0.0050604	0.0071389	0.5677290	32.06382	55.87925	98.94	13.43	334.57	1.00
900	0.0008615	0.0000000	0.0033808	0.2606061	14.83794	55.95469	98.28	6.16	334.98	1.06
940	0.0006488	0.0000000	0.0028325	0.2225905	12.75328	56.42874	98.49	5.26	337.57	1.09
990	0.0009273	0.0006877	0.0050391	0.4029683	23.54200	57.73687	98.83	9.53	344.70	1.03
1040	0.0007803	0.0000000	0.0030514	0.2367947	14.01967	58.22752	98.35	5.60	347.36	1.07
1100	0.0010122	0.0000000	0.0022194	0.1652975	9.71188	56.93955	96.91	3.91	340.36	1.14
1200	0.0011762	0.0000000	0.0021877	0.1530248	8.56978	53.72635	95.94	3.62	322.76	1.22
1400	0.0021110	0.0000000	0.0023189	0.1403173	7.40618	48.33119	91.57	3.32	292.83	1.37

Notes: ^{36}Ar [a], atmospheric ^{36}Ar; ^{37}Ar [Ca], ^{37}Ar derived from Ca; ^{38}Ar [Cl], ^{38}Ar derived from Cl; ^{39}Ar [K], ^{39}Ar derived from K; ^{40}Ar [r], radiogenic ^{40}Ar.

Table 5. *Apatite (U–Th)/He results for samples of the Katebasu gold deposit*

Sample No.	mol ^{238}U	Standard mol ^{238}U	mol ^{232}Th	Standard mol ^{232}Th	mol ^{4}He	Standard mol ^{4}He	F_T	Th/U	T	Res (μm)	eU (ppm)	Cor. Age (Ma)	± 1σ (Ma)	Outlier Detection
17KT02-A1	6.62×10^{-14}	1.24×10^{-15}	6.72×10^{-13}	8.63×10^{-15}	2.82×10^{-14}	3.35×10^{-16}	0.68	10.1	0	46.6	19.4	144.4	7.6	n
17KT02-A2	8.31×10^{-14}	1.32×10^{-15}	1.11×10^{-12}	1.29×10^{-14}	5.75×10^{-14}	6.47×10^{-16}	0.75	13.3	0	60.0	15.4	175.7	9.2	y
17KT02-A3	9.55×10^{-14}	1.50×10^{-15}	6.65×10^{-13}	7.53×10^{-15}	4.10×10^{-14}	4.98×10^{-16}	0.71	7.0	0	49.5	19.3	180.8	9.4	y
17KT02-A4	8.24×10^{-14}	1.44×10^{-15}	6.55×10^{-13}	7.44×10^{-15}	3.58×10^{-14}	4.23×10^{-16}	0.72	7.9	0	53.0	15.8	164.0	8.6	y
Weighted mean age (Sample 17KT02)												172.9	5.2	
17KT03-A1	1.43×10^{-13}	2.23×10^{-15}	9.03×10^{-13}	1.04×10^{-14}	2.93×10^{-14}	3.57×10^{-16}	0.73	6.3	0	55.1	17.7	88.2	4.6	y
17KT03-A2	2.30×10^{-13}	3.59×10^{-15}	1.30×10^{-12}	1.62×10^{-14}	6.10×10^{-14}	7.27×10^{-16}	0.69	5.6	0	46.0	40.2	130.3	6.8	y
17KT03-A3	3.96×10^{-13}	6.11×10^{-15}	2.36×10^{-12}	2.75×10^{-14}	1.00×10^{-13}	1.11×10^{-15}	0.77	5.9	0	64.9	31.3	107.1	5.6	y
17KT03-A4	2.08×10^{-13}	3.25×10^{-15}	1.21×10^{-12}	1.47×10^{-14}	5.19×10^{-14}	6.18×10^{-16}	0.73	5.8	0	54.5	26.2	113.2	5.9	y
Weighted mean age (Sample 17KT03)												105.5	2.8	
17KT06-A1	4.37×10^{-13}	7.06×10^{-15}	2.32×10^{-12}	2.51×10^{-14}	7.51×10^{-14}	8.90×10^{-16}	0.79	5.3	0	68.8	28.3	76.3	4.0	y
17KT06-A2	2.23×10^{-13}	3.40×10^{-15}	1.24×10^{-12}	1.42×10^{-14}	5.21×10^{-14}	5.97×10^{-16}	0.73	5.5	0	54.0	31.8	108.5	5.7	y
17KT06-A3	1.66×10^{-13}	2.51×10^{-15}	8.22×10^{-13}	8.88×10^{-15}	1.10×10^{-14}	1.29×10^{-16}	0.76	5.0	0	60.8	14.9	31.8	1.7	y
17KT06-A4	3.13×10^{-13}	4.90×10^{-15}	1.84×10^{-12}	2.04×10^{-14}	4.06×10^{-14}	4.16×10^{-16}	0.80	5.9	0	75.3	18.5	53.1	2.8	y
Weighted mean age (Sample 17KT06)												-	-	
17KT09-A1	6.13×10^{-13}	9.42×10^{-15}	3.11×10^{-12}	3.46×10^{-14}	1.05×10^{-13}	1.20×10^{-15}	0.82	5.1	0	82.0	21.9	74.9	3.9	y
17KT09-A2	4.34×10^{-13}	7.05×10^{-15}	1.39×10^{-12}	1.55×10^{-14}	6.64×10^{-14}	7.24×10^{-16}	0.77	3.2	0	61.5	26.1	89.1	4.7	y
17KT09-A3	4.44×10^{-13}	6.59×10^{-15}	2.37×10^{-12}	2.66×10^{-14}	1.14×10^{-13}	1.37×10^{-15}	0.76	5.3	0	60.2	36.6	118.3	6.2	y
17KT09-A4	3.46×10^{-13}	5.19×10^{-15}	1.63×10^{-12}	1.82×10^{-14}	1.43×10^{-13}	1.69×10^{-15}	0.77	4.7	0	62.7	26.9	199.1	10.4	n

	mol ^{238}U		mol ^{232}Th		mol ^{4}He		F_T	eU	T	Res		Cor. Age		
Weighted mean age (Sample 17KT09)												87.9	2.7	
17KT13-A1	5.25×10^{-13}	7.93×10^{-15}	2.71×10^{-12}	3.08×10^{-14}	1.60×10^{-13}	1.91×10^{-15}	0.78	5.2	0	67.8	31.4	137.2	7.2	y
17KT13-A2	2.70×10^{-13}	4.32×10^{-15}	1.15×10^{-12}	1.30×10^{-14}	7.55×10^{-14}	8.90×10^{-16}	0.72	4.3	0	50.6	33.1	152.5	8.0	y
17KT13-A3	1.91×10^{-13}	2.92×10^{-15}	9.83×10^{-13}	1.12×10^{-14}	5.80×10^{-14}	6.90×10^{-16}	0.72	5.1	0	52.1	24.6	149.0	7.8	y
17KT13-A4	3.82×10^{-13}	5.79×10^{-15}	1.77×10^{-12}	1.96×10^{-14}	5.19×10^{-14}	6.18×10^{-16}	0.80	4.6	0	73.5	18.1	63.9	3.3	n
Weighted mean age (Sample 17KT13)												145.6	4.4	
17KT15-A2	1.31×10^{-13}	2.02×10^{-15}	6.78×10^{-13}	7.40×10^{-15}	3.82×10^{-14}	4.08×10^{-16}	0.73	5.2	0	54.2	15.1	140.9	7.3	y
17KT15-A3	1.82×10^{-13}	2.76×10^{-15}	9.90×10^{-13}	1.03×10^{-14}	5.36×10^{-14}	6.52×10^{-16}	0.73	5.4	0	53.7	25.0	138.7	7.2	y
17KT15-A4	9.28×10^{-14}	1.52×10^{-15}	5.15×10^{-13}	5.82×10^{-15}	3.22×10^{-14}	3.94×10^{-16}	0.68	5.5	0	45.0	20.0	173.1	9.1	n
17KT15-A5	1.83×10^{-13}	1.23×10^{-14}	9.31×10^{-13}	6.26×10^{-14}	4.96×10^{-14}	5.98×10^{-16}	0.74	5.1	0	56.9	21.8	130.0	9.1	y
Weighted mean age (Sample 17KT15)												137.4	4.5	
17KT21-A1	2.23×10^{-13}	3.44×10^{-15}	7.67×10^{-13}	8.05×10^{-15}	3.30×10^{-14}	3.65×10^{-16}	0.74	3.4	0	55.1	23.0	86.4	4.5	y
17KT21-A2	2.74×10^{-13}	4.23×10^{-15}	1.30×10^{-12}	1.35×10^{-14}	4.90×10^{-14}	5.89×10^{-16}	0.64	4.7	0	39.3	76.7	103.5	5.4	y
17KT21-A3	1.09×10^{-13}	1.70×10^{-15}	4.09×10^{-13}	5.81×10^{-15}	1.47×10^{-14}	1.82×10^{-16}	0.69	3.7	0	45.3	21.5	81.2	4.3	y
17KT21-A4	3.44×10^{-13}	5.06×10^{-15}	1.31×10^{-12}	1.28×10^{-14}	5.75×10^{-14}	7.00×10^{-16}	0.75	3.8	0	57.1	31.0	92.3	4.8	y
Weighted mean age (Sample 17KT21)												89.5	2.3	
17KT22-A1	2.41×10^{-13}	3.88×10^{-15}	4.54×10^{-13}	6.72×10^{-15}	1.43×10^{-14}	1.78×10^{-16}	0.68	1.9	0	43.1	37.0	47.3	2.5	y
17KT22-A2	3.13×10^{-13}	4.78×10^{-15}	3.55×10^{-13}	5.08×10^{-15}	9.65×10^{-15}	1.16×10^{-16}	0.68	1.1	0	41.5	53.6	28.1	1.5	y
17KT22-A3	1.95×10^{-13}	3.00×10^{-15}	3.36×10^{-13}	3.84×10^{-15}	1.47×10^{-14}	1.82×10^{-16}	0.68	1.7	0	42.1	37.2	61.8	3.3	y
17KT22-A4	4.47×10^{-13}	6.79×10^{-15}	5.74×10^{-13}	5.67×10^{-15}	7.71×10^{-15}	8.85×10^{-17}	0.76	1.3	1	57.4	28.4	13.7	0.7	y
Weighted mean age (Sample 17KT22)												-	-	

Notes: mol ^{238}U / ^{232}Th / ^{4}He, molar concentration of ^{238}U / ^{232}Th / ^{4}He, mol/L; F_T, α-ejection correction factor, assuming homogeneous eU distribution (Farley 2000);

T, grain terminations; Res, equivalent spherical radius; eU, effective uranium concentration; Cor. Age, α-ejection corrected age; "n", outlier; "y", non-outlier.

Table 6. *Zircon (U–Th)/He results for samples of the Katebasu gold deposit*

Sample No.	mol ^{238}U	Standard mol ^{238}U	mol ^{232}Th	Standard mol ^{232}Th	mol ^{4}He	Standard mol ^{4}He	F_T	Th/U	T	Res (μm)	eU (ppm)	Cor. Age (Ma)	± 1σ (Ma)	Outlier Detection
17KT07-Z1	2.57×10^{-12}	1.05×10^{-13}	2.46×10^{-12}	8.18×10^{-14}	9.13×10^{-13}	1.14×10^{-14}	0.70	1.0	2	38.6	433.8	317.2	19.5	y
17KT07-Z2	6.23×10^{-12}	2.55×10^{-13}	4.80×10^{-12}	1.59×10^{-13}	2.29×10^{-12}	3.23×10^{-14}	0.74	0.8	2	43.9	731.5	322.9	20.1	y
17KT07-Z3	3.75×10^{-12}	1.53×10^{-13}	3.08×10^{-12}	1.02×10^{-13}	1.25×10^{-12}	1.49×10^{-14}	0.72	0.8	2	41.3	523.6	298.0	18.4	y
17KT07-Z4	5.87×10^{-12}	2.40×10^{-13}	4.46×10^{-12}	1.48×10^{-13}	1.81×10^{-12}	2.56×10^{-14}	0.70	0.8	2	38.8	1052.0	285.4	17.8	y
Weighted mean age (Sample 17KT07)												304.4	9.4	
17KT17-Z1	7.32×10^{-12}	2.99×10^{-13}	5.46×10^{-12}	1.82×10^{-13}	2.15×10^{-12}	3.67×10^{-14}	0.74	0.7	2	44.1	880.6	260.7	16.5	y
17KT17-Z2	3.63×10^{-12}	1.49×10^{-13}	2.55×10^{-12}	8.46×10^{-14}	1.13×10^{-12}	1.41×10^{-14}	0.72	0.7	2	40.9	545.2	285.4	17.8	y
17KT17-Z4	7.35×10^{-12}	3.00×10^{-13}	6.90×10^{-12}	2.32×10^{-13}	2.40×10^{-12}	3.55×10^{-14}	0.76	0.9	2	48.3	692.3	270.3	16.7	y
Weighted mean age (Sample 17KT03)												271.5	9.8	

Notes: mol ^{238}U / ^{232}Th / ^{4}He, molar concentration of ^{238}U / ^{232}Th / ^{4}He, mol/L; F_T, α-ejection correction factor, assuming homogeneous eU distribution (Farley 2000);

T, grain terminations; Res, equivalent spherical radius; eU, effective uranium concentration; Cor. Age, α-ejection corrected age; "n", outlier; "y", non-outlier.
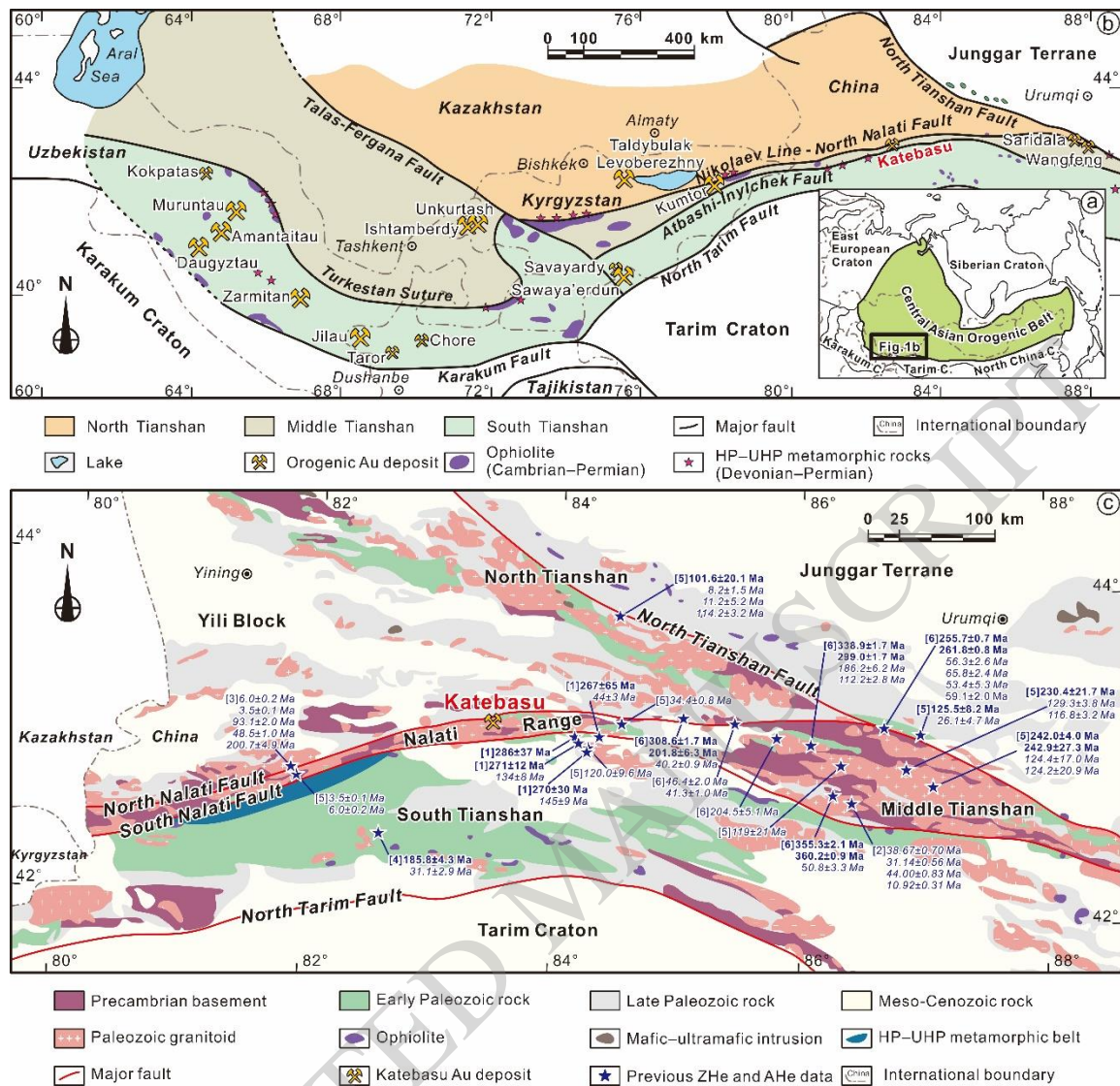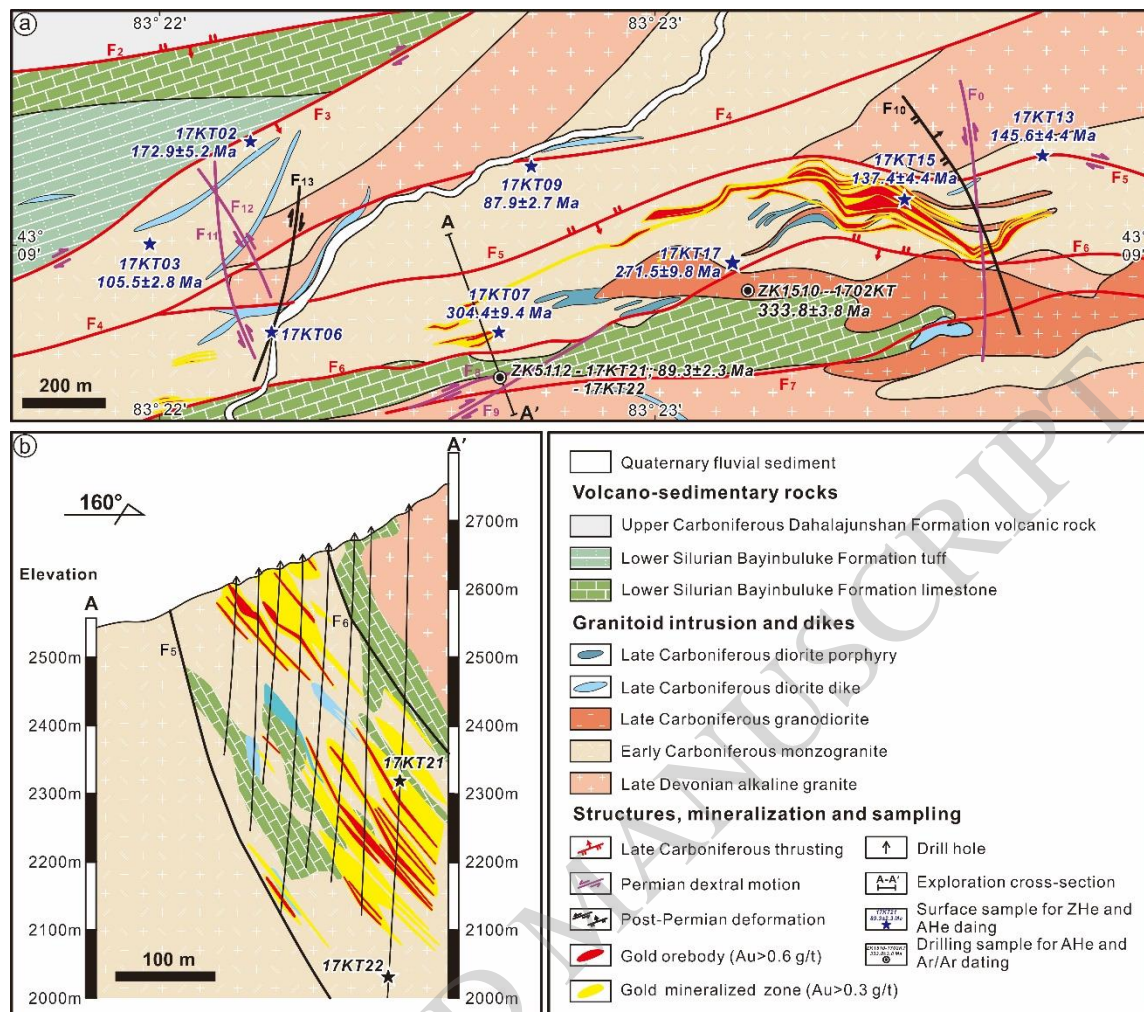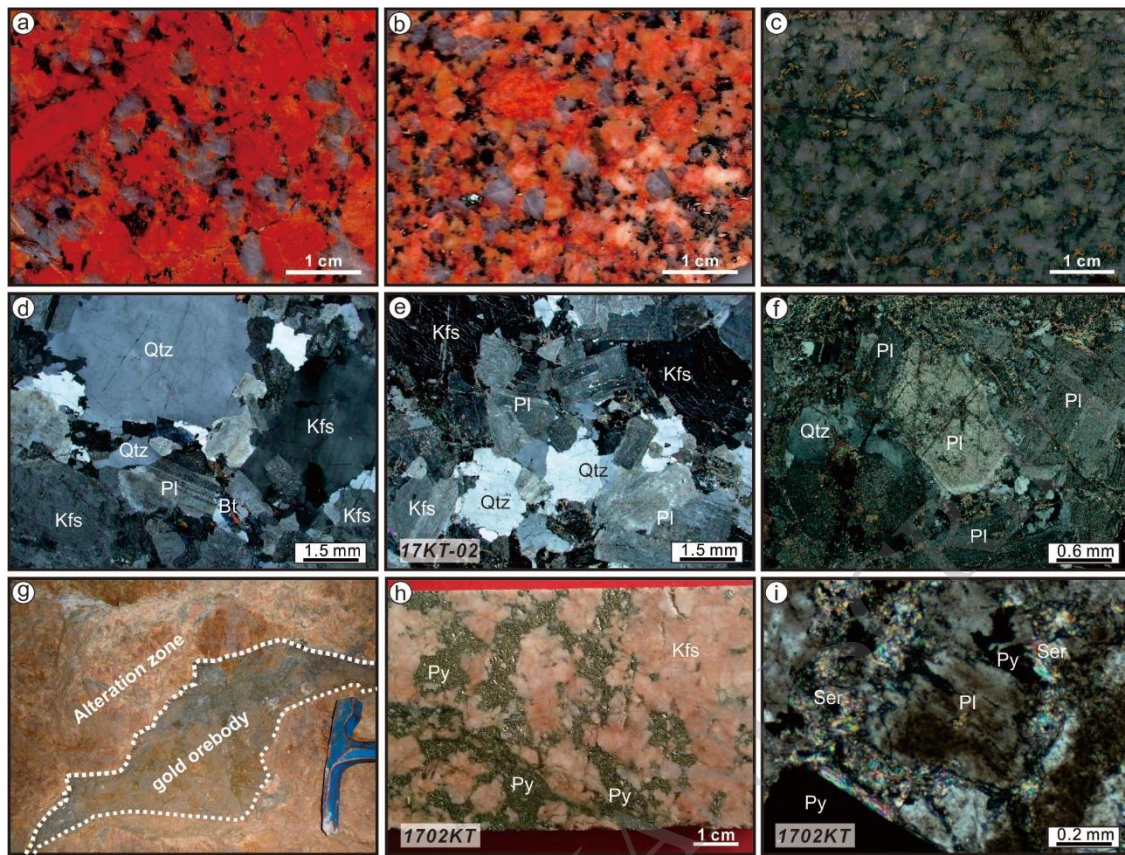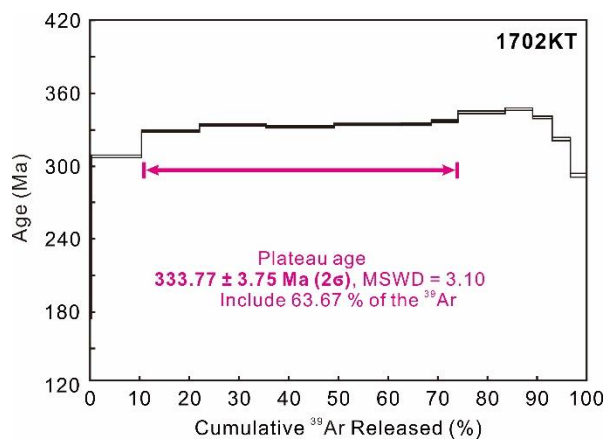
Figure 1

Figure 2

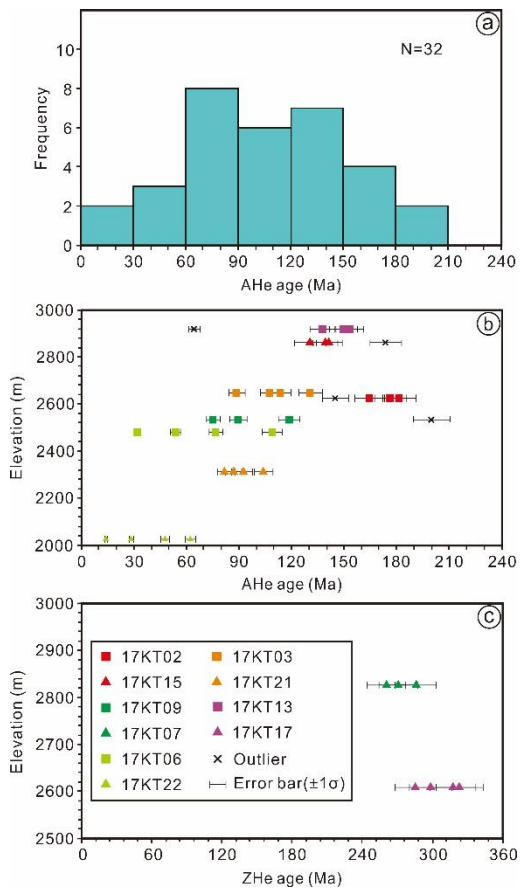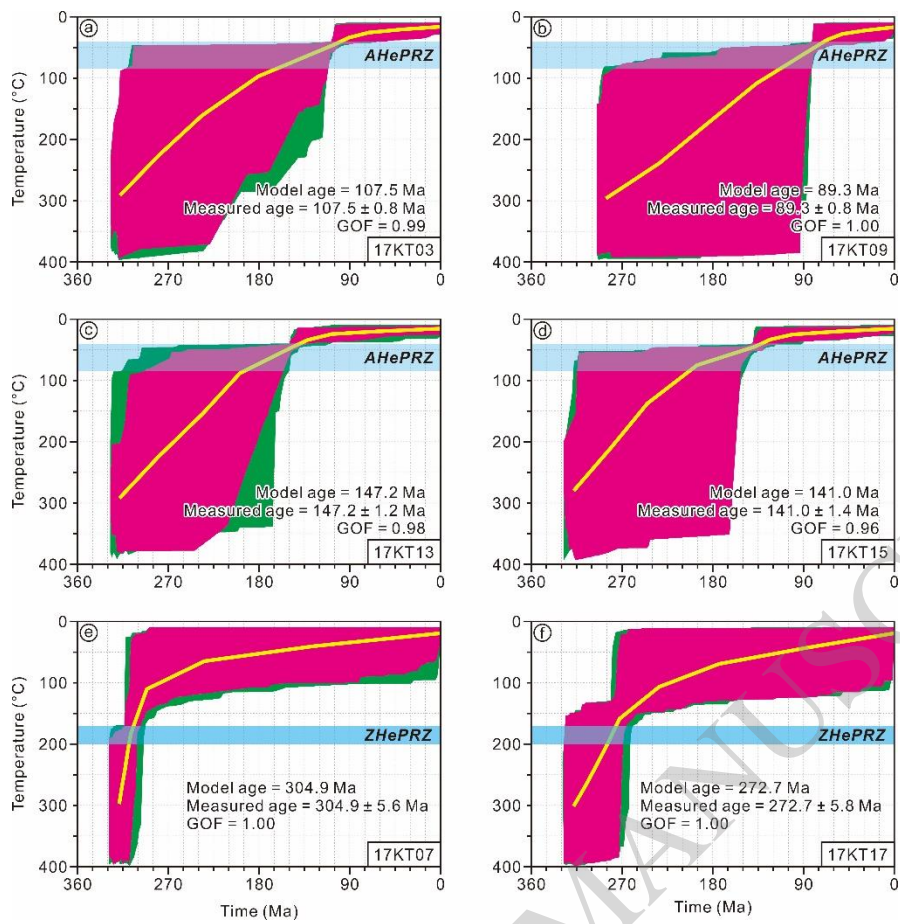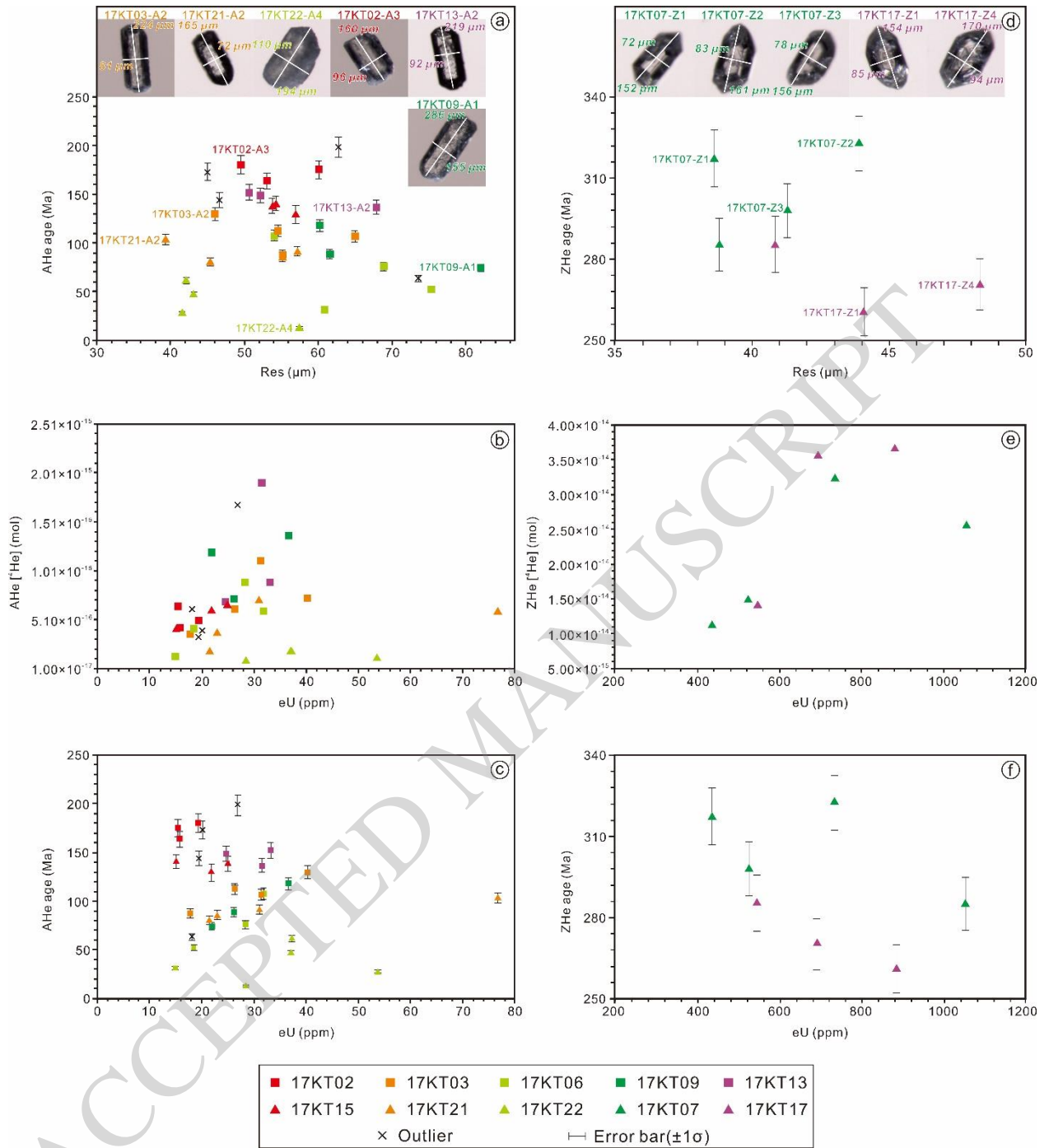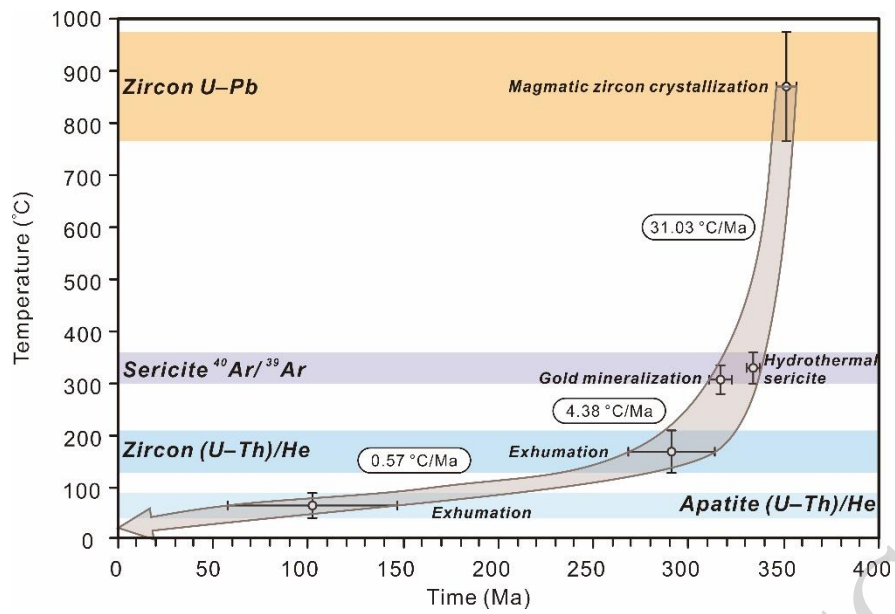**Figure 3**

Figure 4

Figure 5

Figure 6

Figure 7

Figure 8

Figure 9